

Dalton Transactions

Accepted Manuscript



This article can be cited before page numbers have been issued, to do this please use: J. Zhao, J. Liu, J. Yu, Q. Han, Y. Wen and L. Chen, *Dalton Trans.*, 2016, DOI: 10.1039/C6DT03148J.



This is an *Accepted Manuscript*, which has been through the Royal Society of Chemistry peer review process and has been accepted for publication.

Accepted Manuscripts are published online shortly after acceptance, before technical editing, formatting and proof reading. Using this free service, authors can make their results available to the community, in citable form, before we publish the edited article. We will replace this *Accepted Manuscript* with the edited and formatted *Advance Article* as soon as it is available.

You can find more information about *Accepted Manuscripts* in the [Information for Authors](#).

Please note that technical editing may introduce minor changes to the text and/or graphics, which may alter content. The journal's standard [Terms & Conditions](#) and the [Ethical guidelines](#) still apply. In no event shall the Royal Society of Chemistry be held responsible for any errors or omissions in this *Accepted Manuscript* or any consequences arising from the use of any information it contains.

Cite this: DOI: 10.1039/c0xx00000x

www.rsc.org/xxxxxx

ARTICLE TYPE

First quadruple-glycine bridging mono-lanthanide-substituted borotungstate hybrids

Jiancai Liu,^a Jing Yu,^a Qing Han,^a Yue Wen,^a Lijuan Chen^{a,*} and Junwei Zhao^{a,b,*}

Received (in XXX, XXX) Xth XXXXXXXXX 20XX, Accepted Xth XXXXXXXXX 20XX

DOI: 10.1039/b000000x

A class of novel organic–inorganic hybrid lanthanide (Ln)-substituted Keggin-type borotungstates $K_4Na_4H_4[Ln_2(gly)_4(\alpha-BW_{11}O_{39})_2] \cdot 23H_2O$ [Ln = Ce³⁺ (**1**), Pr³⁺ (**2**), Nd³⁺ (**3**), Sm³⁺ (**4**), Eu³⁺ (**5**), Tm³⁺ (**6**); gly = glycine] have been synthesized from the reaction of $K_8[BW_{11}O_{39}H] \cdot 13H_2O$, NaAc \cdot 6H₂O and $Ln(NO_3)_3 \cdot 6H_2O$ by employing gly ligands as structure-stabilizing agents in the conventional aqueous solution system and structurally characterized by elemental analyses, IR spectra, thermogravimetric (TG) analyses, power X-ray diffraction (PXRD) and single-crystal X-ray diffraction. The common prominent structural feature of isomorphous **1–6** is that they all consist of two mono-Ln-substituted Keggin $[Ln(\alpha-BW_{11}O_{39})]^{6-}$ fragments linked by four gly ligands furnishing an intriguing dimeric assembly of the quadruple-gly-connective mono-Ln-substituted borotungstate, in which each carboxylic oxygen atom from gly ligands is bound to Ln³⁺ cations in the μ_2 -O or μ_3 -O mode. To the best of our knowledge, **1–6** represent the first examples of inorganic–organic hybrid Ln-substituted borotungstates functionalized by quadruple amino acid bridges. The solid-state photoluminescence properties of **3–5** have been carried out at ambient temperature and the photoluminescence emission spectra exhibit the characteristic emission bands derived from Ln³⁺ centers. The thermostability of **1–6** has been studied and the thermal decomposition procedure of **3** is comprehensively investigated by the assistance of variable-temperature PXRD patterns and variable-temperature IR spectra. Furthermore, the magnetic susceptibility measurements of **1**, **2** and **4** have been conducted.

Introduction

Polyoxometalates (POMs) are early transition metal oxide anionic clusters constructed from transition metals in their high oxidation states (primarily Mo^{VI}, W^{VI}, V^V, Nb^V and Ta^{IV}), which exhibit unrivalled structural diversities, seductive properties and underling applications in catalysis, magnetism, medicine, materials science and nanotechnology.¹ In particular, polyoxotungstates (POTs), as a large subclass of POM chemistry, are always utilized as multifunctional inorganic polydentate O-donor candidates to accommodate oxophilic d- or f-block metals for the construction of transition metal (TM) or Ln substituted POTs on account of their highly negative charged and O-enriched surface. Hitherto, a tremendous number of TM-substituted POTs have been dug out since the first example was addressed by Simmons in 1962 and its structure that was composed of an 11-tungstosilicate wherein one W atom of the Keggin structure was replaced by a Co²⁺ ion was determined by St. Moritz in 1966.² In contrast, the development of Ln-substituted POTs (LSPs) is relatively laggardly. Historically, in 1914, Barbieri initiated the study of the reaction of polyoxoanions and Ln³⁺ ions with the discovery of the first Ln-substituted POM $(NH_4)_2[H_6CeMo_{12}O_{42}] \cdot nH_2O$ ³ and after a long-standing sluggish period, until 1971, Peacock and Weakley succeeded in obtaining a series of LSPs $[Ln(W_5O_{18})_2]^{n-}$ and synchronously explored the reactivity of Ln^{3+/4+} cations with monolacunary Keggin-type $[XW_{11}O_{39}]^{n-}$ (X = Si^{IV}, P^V) and Dawson-type $[P_2W_{17}O_{61}]^{10-}$ polyoxoanions, giving rise to 1:1- or 1:2-type Keggin or Dawson LSPs.⁴ These preliminary discoveries are undoubtedly the extremely significant pioneering work, which not only shed light on the great possibilities in implanting Ln³⁺ cations into various POT precursors, but also open the way for discovering

neoteric LSPs. Henceforth, numerous LSPs have been reported over the past few decades, which possess aesthetic structures as well as potential applications such as magnetism, photoluminescence and catalysis.⁵

Among LSPs, organic-ligand-functionalized Ln-substituted lacunary Keggin- or Dawson-type POTs have been also investigated.^{5d–v} Notably, the research on the incorporation of organic ligands into the Ln–POT system has aroused increasing interest in that organic linkers can somewhat facilitate the agglomeration of Ln³⁺ centers to form polynuclear species, which are principally concentrated on the overwhelming variety of carboxylate ligands from monocarboxylic components (acetate, nicotinic acid, pyridine-4-carboxylic acid) to multicarboxylic components (tartrate, pyridinedicarboxylic, citric acid),^{5d–v} however, amino acid ligands have been little employed in this respect and only few examples containing gly, alanine (ala) or proline (pro) have been reported to date.⁶ For instance, in 2007, Wang et al. first obtained an unusual ala-decorated quadrmeric crytand-type arsenotungstate $[Ce_4As_4W_{44}O_{151}(ala)_4(OH)_2(H_2O)_{10}]^{12-}$,^{6a} afterwards, their group successfully synthesized a strand of 1-D chainlike aggregates $[Ln_6(H_2O)_x\{As_4W_{44}(OH)_2(pro)_2O_{151}\}]^{10-}$ (Ln = Tb³⁺, Dy³⁺, Nd³⁺) built by the crown-shape units $[Ln_4(H_2O)_x\{As_4W_{44}(OH)_2(pro)_2O_{151}\}]^{16-}$ that are stabilized by pro ligands linked by two extra hydrated Ln³⁺ cations.^{6b} Noticeably, Boskovic's group conducted a set of research on the reactivity of Ln³⁺ cations with arsenotungstates in the participation of gly affording a new family of gly-based LSPs such as the 1-D chain $[Dy_4As_2W_{22}O_{76}(H_2O)_{19}(C_2H_5NO_2)_2]^{2-}$ (C₂H₅NO₂ = glycine) as well as discrete tetrameric species $[As_4(YW_3)W_{44}Y_4O_{159}(gly)_8(H_2O)_{14}]^{9-}$ and $[Ln_4As_5W_{40}O_{144}(H_2O)_{10}(gly)_2]^{21-}$ (Ln = Gd³⁺, Tb³⁺, Dy³⁺, Ho³⁺, Y³⁺).^{6c–e} Naruke and coworkers also accelerated the development of gly-functionalized LSPs with attaining two chiral enantiopure complexes

$K_{1.3}Na_{3.2}H_{6.5}[L-Pr(PW_{11}O_{39})_2] \cdot 8.3L-pro \cdot 21.5H_2O$ and $K_{1.3}Na_{3.2}H_{6.5}[D-Pr(PW_{11}O_{39})_2] \cdot 8.3D-pro \cdot 17H_2O$ by using L- and D-pro as chiral auxiliary agents.^{6f} Very recently, our group made an pro-modified dimericphosphotungstate $KNa_3[HPRO]_7[Sm(\alpha-PW_{11}O_{39})_2] \cdot Pro \cdot 18H_2O$ and characterized its ferroelectric behavior.^{6g} Nevertheless, examples of Ln-substituted borotungstates (BTs) are not reported as extensively as phosphotungstates or arsenotungstates.^{5k,7} Some inchoate reports have emerged with the discovery of 1:1-type complexes $[Ln(BW_{11}O_{39})(H_2O)_3]^{6-}$ (Ln = Sm^{3+} , Eu^{3+} , Tb^{3+} , Dy^{3+}) as well as 1:2-type complexes $[Ln(BW_{11}O_{39})_2]^{15-}$ and $[Ln(BW_{11}O_{39})(W_5O_{18})]^{12-}$ (Ln = Ce^{3+} , Eu^{3+}).^{7a-d} Furthermore, some extended structures from 1-D $[Ce_2(BW_{11}O_{39})_2(H_2O)_6]^{12-}$ and $\{[Ho_4(dpdo)_8(H_2O)_{16}BW_{12}O_{40}](H_2O)_2\}^{7+}$ (dpdo = 4,4'-bipyridine-N,N'-dioxide hydrate)^{7e-f} to 3-D $[LnK(H_2O)_{12}][Ln(H_2O)_6]_2[(H_2O)_4LnBW_{11}O_{39}H]_2 \cdot 20H_2O$ (Ln = Ce^{3+} , Nd^{3+}) and $\{[(C_6NO_2H_5)Ln(H_2O)_5]_2[(H_2O)_4LnBW_{11}O_{39}H]_2\}^{4-}$ (Ln = Ce^{3+} , Nd^{3+} , $C_6NO_2H_5$ = pyridine-4-carboxylic acid) were also resoundingly separated.^{5k} These sporadic examples not only hint the great difficulty and challenge in preparing novel Ln-substituted BTs (LSBs), but also pave the way for discovering other BT-based functional materials.

As far as we know, BTs delegate a category of species with unusual properties in comparison with the common silicotungstate and phosphotungstate analogues,⁸ partly because that the B^{III} heteroatoms owning the lowest charge and the smallest size can probably define some distinctive properties,⁹ and the electron-deficient B^{III} atoms can adopt either trigonal or tetrahedral coordination modes.¹⁰ These unique features inspired us to have a close insight into it. Considering that no examples of LSBs containing amino acid ligands have been reported to date, it is of particular interest for us to explore an appropriate approach to introduce amino acid ligands and various Ln³⁺ cations into the BT system for obtaining a myriad of manifold LSBs with diverse functionalities. It is well known that Ln³⁺ ions behaving as hard acids with the high coordination numbers and the strong oxophilic characteristic are apt to coalesce with oxygenic ligands such as POM frameworks, and their fascinating photophysical and magnetic properties make them popular in the aspect of potential applications. What's more, amino acid ligands own flexible carboxyl and amino coordination sites as well as the inclusion of them can bridge and stabilize the final structures whilst the in-situ assembly of lacunary POT precursor under conventional aqueous conditions has been developed as an efficient and ubiquitous method in constructing novel LSPs. On the base of these considerations, we launched the exploration on the assembly reactions of BT precursors with Ln³⁺ cations in the participation of amino acid ligands and thus a family of quadruple-gly bridging LSBs $K_4Na_4H_4[Ln_2(gly)_4(\alpha-BW_{11}O_{39})_2] \cdot 23H_2O$ [Ln = Ce^{3+} (**1**), Pr^{3+} (**2**), Nd^{3+} (**3**), Sm^{3+} (**4**), Eu^{3+} (**5**), Tm^{3+} (**6**); gly = glycine] were harvested, delegating the first examples of inorganic-organic hybrid BTs based on Ln³⁺ cations and amino acid linkers. Furthermore, the photoluminescence (PL) properties and lifetime decay behaviors of **3–5** have been studied, indicating that their PL behaviors are mainly derived from the characteristic emissions from Ln³⁺ centers. The lifetime of **4** originates from the combined action of Ln³⁺ cations and BT segments whereas the lifetimes of **3** and **5** chiefly originate from Ln³⁺ cations. The magnetic measurements of **1**, **2** and **4** have been performed between 1.8 and 300 K. The declining of $\chi_M T$ values of **1** and **4** with decreasing

temperature can principally be due to the antiferromagnetic couplings interactions within magnetic centers as well as the thermal depopulation of the Stark levels whereas the magnetic behavior of **2** may primarily be ascribed to the thermal progressive depopulation of the Stark levels of Pr^{3+} ions. In addition, the TG analyses of **1–6** have been probed and the thermal decomposition process of **3** is intensively investigated by the multiply dynamic analyses including TG curve, variable-temperature PXRD patterns and variable-temperature IR spectra.

Experimental

Materials and physical measurements

The precursor $K_8[\alpha-BW_{11}O_{39}H] \cdot 13H_2O$ was synthesized according to the literature method^{9a} and characterized by IR spectroscopy. All other chemicals were used as purchased without further purification. C, H and N elemental analyses were conducted on a Perkin-Elmer 2400-II CHNS/O analyzer. Inductively coupled plasma atomic emission spectrometry (ICP-AES) were performed on a Perkin-Elmer Optima 7500 ICP-AES spectrometer. IR spectra were recorded on a Bruker VERTEX 70 IR spectrometer using KBr pellets in the range of 4000–400 cm^{-1} . PXRD patterns were collected on a Bruker AXS D8 Advance diffractometer instrument with Cu K α radiation (λ = 1.54056 Å) at 293 K. TG analyses were performed on a Mettler-Toledo TGA/SDTA 851e instrument under a N₂ atmosphere with a heating rate of 10 °C min⁻¹ from 25 to 800 °C. The magnetic experiments were carried out on a Quantum Design SQUID (MPMS-XL 7). PL spectra, lifetime decay behaviors and luminescence quantum yields were performed in the solid state at ambient temperature on an Edinburgh FLS 980 Analytical Instrument equipped with a 450 W xenon lamp and a $\mu F900H$ high-energy microsecond flash lamp as the excitation source.

Preparations of 1–6

$K_4Na_4H_4[Ce_2(gly)_4(\alpha-BW_{11}O_{39})_2] \cdot 23H_2O$ (1**).** $K_8[\alpha-BW_{11}O_{39}H] \cdot 13H_2O$ (3.006 g, 0.938 mmol) and NaAc $\cdot 3H_2O$ (0.525 g, 3.858 mmol) were dissolved in 20 mL distilled water under stirring and the pH of the solution was adjusted to 2.7 by 6 mol L⁻¹ HCl. After the solution was stirred for ca. 20 min, $Ce(NO_3)_3 \cdot 6H_2O$ (0.207 g, 0.477 mmol) and gly (0.196 g, 2.610 mmol) were successively added and the pH value was adjusted to 2.7 again by using 6 mol L⁻¹ NaOH. The resulting solution was stirred for another 30 min, kept in the 90 °C water bath for 2 h and filtered when it cooled to room temperature. Slow evaporation of the filtrate at room temperature led to the yellow needle crystals of **1** in about two weeks. Yield: 0.37 g (23.3%) based on $Ce(NO_3)_3 \cdot 6H_2O$. Elemental analysis (%) calcd: C, 1.46; H, 1.07; N, 0.85; Na, 1.40; K, 2.38; W, 61.64; Ce, 4.27. Found: C, 1.35; H, 1.17; N, 0.76; Na, 1.62; K, 2.21; W, 61.50; Ce, 4.39. IR (KBr, cm^{-1}): 3418(s), 1621(m), 1477(m), 1416(w), 948(m), 822(s), 691(w), 523(m), 427(w) (Fig. S1).

$K_4Na_4H_4[Pr_2(gly)_4(\alpha-BW_{11}O_{39})_2] \cdot 23H_2O$ (2**).** The synthetic procedure of **2** is similar to **1** except that $Ce(NO_3)_3 \cdot 6H_2O$ (0.207 g, 0.477 mmol) was replaced by $Pr(NO_3)_3 \cdot 6H_2O$ (0.207 g, 0.477 mmol). Green needle crystals of **2** were obtained. Yield: 0.32 g (20.1%) based on $Pr(NO_3)_3 \cdot 6H_2O$. Elemental analysis (%) calcd: C, 1.46; H, 1.07; N, 0.85; Na, 1.40; K, 2.38; W, 61.63; Pr, 4.29. Found: C, 1.43; H, 1.18;

Table 1 X-ray diffraction crystallographic data and structure refinements for 1–6.

	1	2	3	4	5	6
Empirical formula	C ₈ H ₇₀ B ₂ K ₄ Na ₄ Na ₄ Ce ₂ O ₁₀₉ W ₂₂	C ₈ H ₇₀ B ₂ K ₄ Na ₄ Na ₄ Pr ₂ O ₁₀₉ W ₂₂	C ₈ H ₇₀ B ₂ K ₄ Na ₄ Na ₄ Nd ₂ O ₁₀₉ W ₂₂	C ₈ H ₇₀ B ₂ K ₄ Na ₄ Na ₄ Sm ₂ O ₁₀₉ W ₂₂	C ₈ H ₇₀ B ₂ K ₄ Na ₄ Na ₄ Eu ₂ O ₁₀₉ W ₂₂	C ₈ H ₇₀ B ₂ K ₄ Na ₄ Na ₄ Tm ₂ O ₁₀₉ W ₂₂
Formula weight	6561.60	6563.18	6569.84	6582.06	6585.28	6619.22
Crystal system	Monoclinic	Monoclinic	Monoclinic	Monoclinic	Monoclinic	Monoclinic
Space group	<i>P</i> 2(1)/ <i>c</i>	<i>P</i> 2(1)/ <i>c</i>	<i>P</i> 2(1)/ <i>c</i>	<i>P</i> 2(1)/ <i>c</i>	<i>P</i> 2(1)/ <i>c</i>	<i>P</i> 2(1)/ <i>c</i>
<i>a</i> , Å	11.783(2)	11.7518(9)	11.7456(8)	11.7598(7)	11.7069(7)	11.6408(10)
<i>b</i> , Å	21.459(4)	21.4795(16)	21.6247(15)	21.7014(14)	21.6010(13)	21.7217(18)
<i>c</i> , Å	21.350(4)	21.3507(17)	21.5977(15)	21.7560(14)	21.3932(14)	21.4679(19)
α , deg	90	90	90	90	90	90
β , deg	91.787(3)	91.9080(10)	92.4380(10)	92.4250(10)	92.3710(10)	92.451(2)
γ , deg	90	90	90	90	90	90
<i>V</i> , Å ³	5395.9(17)	5386.4(7)	5480.7(7)	5547.2(6)	5405.3(6)	5423.4(8)
<i>Z</i>	2	2	2	2	2	2
μ , mm ^{−1}	24.457	24.559	24.195	24.028	24.733	25.130
<i>F</i> (000)	5784	5788	5792	5800	5804	5828
<i>T</i> , K	296(2)	296(2)	296(2)	296(2)	296(2)	296(2)
Limiting indices	−13 ≤ <i>h</i> ≤ 13 −19 ≤ <i>k</i> ≤ 25 −25 ≤ <i>l</i> ≤ 24	−13 ≤ <i>h</i> ≤ 13 −25 ≤ <i>k</i> ≤ 17 −25 ≤ <i>l</i> ≤ 24	−13 ≤ <i>h</i> ≤ 13 −25 ≤ <i>k</i> ≤ 25 −21 ≤ <i>l</i> ≤ 25	−13 ≤ <i>h</i> ≤ 13 −22 ≤ <i>k</i> ≤ 25 −24 ≤ <i>l</i> ≤ 25	−13 ≤ <i>h</i> ≤ 13 −25 ≤ <i>k</i> ≤ 20 −25 ≤ <i>l</i> ≤ 25	−13 ≤ <i>h</i> ≤ 13 −23 ≤ <i>k</i> ≤ 25 −25 ≤ <i>l</i> ≤ 25
No. of reflections collected	26214	27048	27696	27769	27009	27540
No. of independent reflections	9217	9363	9600	9609	9396	9511
<i>R</i> _{int}	0.0885	0.0636	0.0508	0.0758	0.0498	0.0669
Data/restraints/parameters	9217 / 180 / 674	9363 / 42 / 680	9600 / 84 / 697	9609 / 66 / 692	9396 / 24 / 681	9511 / 31 / 682
GOF on <i>F</i> ²	1.020	1.038	1.024	1.009	1.010	1.026
Final <i>R</i> indices	<i>R</i> ₁ = 0.0579 <i>wR</i> ₂ = 0.1310	<i>R</i> ₁ = 0.0405 <i>wR</i> ₂ = 0.0724	<i>R</i> ₁ = 0.0334 <i>wR</i> ₂ = 0.0791	<i>R</i> ₁ = 0.0429 <i>wR</i> ₂ = 0.0654	<i>R</i> ₁ = 0.0352 <i>wR</i> ₂ = 0.0811	<i>R</i> ₁ = 0.0435 <i>wR</i> ₂ = 0.0856
<i>R</i> indices (all data)	<i>R</i> ₁ = 0.0886 <i>wR</i> ₂ = 0.1417	<i>R</i> ₁ = 0.0674 <i>wR</i> ₂ = 0.0780	<i>R</i> ₁ = 0.0439 <i>wR</i> ₂ = 0.0827	<i>R</i> ₁ = 0.0779 <i>wR</i> ₂ = 0.0717	<i>R</i> ₁ = 0.0472 <i>wR</i> ₂ = 0.0849	<i>R</i> ₁ = 0.0731 <i>wR</i> ₂ = 0.0932
Largest diff. peak and hole, e [−] Å ^{−3}	4.140, −3.155	2.146, −1.681	2.132, −1.838	3.961, −2.173	2.145, −1.761	2.227, −1.606

N, 0.74; Na, 1.55; K, 2.24; W, 61.75; Pr, 4.18. IR (KBr, cm^{−1}): 3410(s), 1621(m), 1469(m), 1414(w), 947(m), 819(s), 691(w), 517(m), 428(w) (Fig. S1).

K₄Na₄H₄[Nd₂(gly)₄(α-BW₁₁O₃₉)₂]·23H₂O (3). The synthetic procedure of **3** is similar to **1** except that Ce(NO₃)₃·6H₂O (0.207 g, 0.477 mmol) was replaced by Nd(NO₃)₃·6H₂O (0.207 g, 0.472 mmol). Purple needle crystals of **3** were obtained. Yield: 0.41 g (25.8%) based on Nd(NO₃)₃·6H₂O. Elemental analysis (%) calcd: C, 1.46; H, 1.07; N, 0.85; Na, 1.40; K, 2.38; W, 61.56; Nd, 4.39. Found: C, 1.51; H, 1.10; N, 0.78; Na, 1.61; K, 2.21; W, 61.47; Nd, 4.49. IR (KBr, cm^{−1}): 3433(s), 1645(m), 1476(m), 1412(w), 946(m), 819(s), 697(w), 518(m), 430(w) (Fig. S1).

K₄Na₄H₄[Sm₂(gly)₄(α-BW₁₁O₃₉)₂]·23H₂O (4). The synthetic procedure of **4** is similar to **1** except that Ce(NO₃)₃·6H₂O (0.207 g, 0.477 mmol) was replaced by Sm(NO₃)₃·6H₂O (0.207 g, 0.466 mmol). Pale yellow needle crystals of **4** were obtained. Yield: 0.35 g (22.1%) based on Sm(NO₃)₃·6H₂O. Elemental analysis (%) calcd: C, 1.46; H, 1.07; N, 0.85; Na, 1.40; K, 2.38; W, 61.45; Sm, 4.57. Found: C, 1.53; H, 1.12; N, 0.73; Na, 1.60; K, 2.21; W, 61.34; Sm, 4.45. IR (KBr, cm^{−1}): 3394(s), 1621(m), 1477(m), 1412(w), 948(m), 826(s), 702(w), 512(m), 430(w) (Fig. S1).

K₄Na₄H₄[Eu₂(gly)₄(α-BW₁₁O₃₉)₂]·23H₂O (5). The synthetic procedure of **5** is similar to **1** except that Ce(NO₃)₃·6H₂O (0.207 g, 0.477 mmol) was replaced by Eu(NO₃)₃·6H₂O (0.207 g, 0.464 mmol). Colorless needle crystals of **5** were obtained. Yield: 0.29 g (18.2%)

based on Eu(NO₃)₃·6H₂O. Elemental analysis (%) calcd: C, 1.46; H, 1.07; N, 0.85; Na, 1.40; K, 2.38; W, 61.42; Eu, 4.62. Found: C, 1.42; H, 1.18; N, 0.79; Na, 1.57; K, 2.47; W, 61.28; Eu, 4.50. IR (KBr, cm^{−1}): 3433(s), 1645(m), 1476(m), 1412(w), 946(m), 821(s), 697(w), 519(m), 431(w) (Fig. S1).

K₄Na₄H₄[Tm₂(gly)₄(α-BW₁₁O₃₉)₂]·23H₂O (6). The synthetic procedure of **6** is similar to **1** except that Ce(NO₃)₃·6H₂O (0.207 g, 0.477 mmol) was replaced by Tm(NO₃)₃·6H₂O (0.207 g, 0.461 mmol). Colorless needle crystals of **6** were obtained. Yield: 0.31 g (19.5%) based on Tm(NO₃)₃·6H₂O. Elemental analysis (%) calcd: C, 1.45; H, 1.07; N, 0.85; Na, 1.39; K, 2.36; W, 61.10; Tm, 5.10. Found: C, 1.48; H, 1.13; N, 0.76; Na, 1.50; K, 2.17; W, 61.21; Tm, 4.92. IR (KBr, cm^{−1}): 3442(s), 1645(m), 1477(m), 1413(w), 947(m), 826(s), 700(w), 519(m), 430(w) (Fig. S1).

X-ray crystallography

Single-crystal X-ray diffraction data of **1–6** were collected on a Bruker APEX-II CCD detector at 296(2) K with graphite monochromated Mo *K*α radiation (λ = 0.71073 Å). Their structures were determined by direct methods and refined on *F*² by full-matrix least-squares method using the SHELXTL-97 program package.¹¹ The remaining atoms were found from successive full-matrix least-squares refinements on *F*² and Fourier syntheses. Lorentz polarization and SADABS corrections were applied. All hydrogen atoms attached to carbon and nitrogen atoms were geometrically placed and refined isotropically as a riding model using the default

SHELXTL parameters. No hydrogen atoms associated with water molecules were located from the difference Fourier map. All non-hydrogen atoms were refined anisotropically. The structural refinement details in 1–6 are seen in ESI. The X-ray diffraction crystallographic data and structure refinements for 1–6 are demonstrated in Table 1. Crystallographic data for 1–6 reported in this paper have been deposited in the Cambridge Crystallographic Data Centre with CCDC 1495658–1495663 for 1–6. These data can be obtained free of charge from the Cambridge Crystallographic Data Centre via www.ccdc.cam.ac.uk/data_request/cif.

Results and discussion

Syntheses

LSPs have witnessed the tremendous development in the past several decades.^{5–6} However, it is still in its infancy in exploiting the realm of LSBs. In this paper, the monovacant precursor $K_8[\alpha\text{-BW}_{11}\text{O}_{39}\text{H}]\cdot 13\text{H}_2\text{O}$ was selected as the original material to react with Ln^{3+} cations in the existence of gly ligands in the aqueous solution and a strand of organic–inorganic hybrid LSBs 1–6 were triumphantly obtained. On the basis of the survey about the previously reported literatures, it can be easily found that rare examples on LSPs functionalized by amino acid ligands (Table 2) are reported and mainly confined to arsenotungstates and phosphotungstates though many inorganic–organic hybrid LSPs involving carboxylic acid ligands have been covered. Having a close observation on the synthetic methods, preliminary information on the reaction system is gained that an acidic reaction medium can contribute to the aggregation of Ln^{3+} cations, amino acid ligands and POM fragments to produce alluring and complicated architectures. Recently, our group have conducted some researches on the reaction of POMs with TM and / or Ln^{3+} cations in the presence of amino acids and some progresses have been achieved, such as the 1-D polymolybdates with copper-arg linkers $[\text{Cu}(\text{arg})_2]_2[(\text{CuO}_6)\text{Mo}_6\text{O}_{18}(\text{As}_3\text{O}_3)_2]\cdot 4\text{H}_2\text{O}$ and $[\text{Cu}(\text{arg})_2]_3[\text{TeMo}_6\text{O}_{24}]\cdot 8\text{H}_2\text{O}$ (arg = L-arginine),¹² and the dimeric thr-decorated heterometallic species $[\text{Ln}(\text{H}_2\text{O})_8]_2[\text{Fe}_4(\text{H}_2\text{O})_8(\text{thr})_2][\text{B}\beta\text{-XW}_9\text{O}_{33}]_2\cdot n\text{H}_2\text{O}$ (X = Sb^{III} , As^{III}).¹³ Enlightened by the previous achievements, we tried to introduce gly ligand into the Ln/BTs system and finally separated the first type of dimeric LSBs bridged by four gly connectors $K_4\text{Na}_4\text{H}_4[\text{Ln}_2(\text{gly})_4(\alpha\text{-BW}_{11}\text{O}_{39})_2]\cdot 23\text{H}_2\text{O}$ [Ln

= Ce^{3+} (1), Pr^{3+} (2), Nd^{3+} (3), Sm^{3+} (4), Eu^{3+} (5), Tm^{3+} (6)] by means of the aqueous solution method. It's worth mentioning that, in the case of our synthetic approach, the reaction reagent and the pH value play an imperative role in the formation of the desired products. On the one hand, the usage amount of $K_8[\alpha\text{-BW}_{11}\text{O}_{39}\text{H}]\cdot 13\text{H}_2\text{O}$ precursor from 2.5 g to 3.0 g is advantageous for improving the yield of the desired compounds. On the other hand, the pH value of 2.4 – 3.5 is helpful for the generation of target compounds as in this circumstance the acidic reaction environment is essential to avoid the hydrolysis of Ln^{3+} ions and favors the incorporation of gly molecules. Furthermore, the inclusion of gly molecules not only is anticipated to reduce the possibilities of forming precipitations between Ln^{3+} ions and $[\alpha\text{-BW}_{11}\text{O}_{39}]^{9-}$ fragments, but also can stabilize the final structures.

Structural description

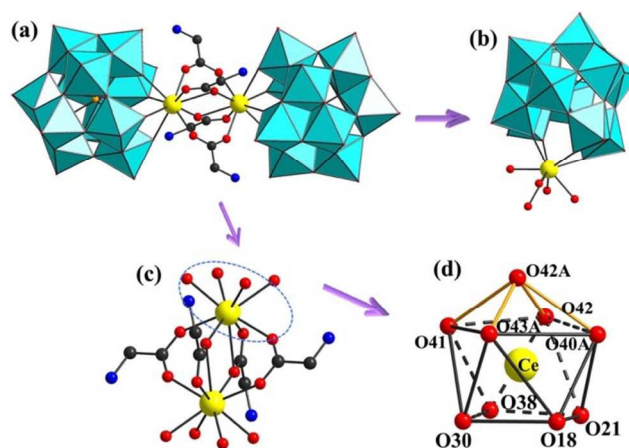


Fig. 1 (a) View of the molecular structure of 1 with the selected labeling scheme. (b) Incorporation of the Ce^{3+} ion into the monolacunary Keggin $[\alpha\text{-BW}_{11}\text{O}_{39}]^{9-}$ fragment. (c) The connection between two Ce^{3+} ions and gly ligands in 1. (d) The coordination sphere of the Ce^{3+} ion in 1. The atoms with the suffix A are generated by the symmetry operation where A: 1-x, 1-y, 1-z. C: gray-80%, N: blue, O: red, Ce: yellow, B: light orange, $\{\text{WO}_6\}$: turquoise.

Table 2. Summary of LSPs functionalized by amino acid molecules.

Year	Phases	Major reactants	pH	Synthetic methods
2007	$[\text{Ce}_4\text{As}_4\text{W}_{44}\text{O}_{151}(\text{ala})_4(\text{OH})_2(\text{H}_2\text{O})_{10}]^{12-6a}$	$\text{K}_9\text{Na}_7[\{\text{Ce}_2\text{O}(\text{H}_2\text{O})_5\}\{\text{WO}(\text{H}_2\text{O})\}\{\text{AsW}_9\text{O}_{33}\}_2]_2\cdot 19.5\text{H}_2\text{O}$ /ala	2.0	aqueous method
2010	$[\text{Dy}_4\text{As}_2\text{W}_{22}\text{O}_{76}(\text{H}_2\text{O})_{19}(\text{C}_2\text{H}_5\text{NO}_2)_2]^{2-6c}$	$\text{Dy}(\text{NO}_3)_3\cdot \text{H}_2\text{O}/\text{gly}/\text{K}_{14}[\text{As}_2\text{W}_{19}\text{O}_{67}(\text{H}_2\text{O})]$	1.55	aqueous method
2011	$[\text{Ln}_4\text{As}_5\text{W}_{40}\text{O}_{144}(\text{H}_2\text{O})_{10}(\text{gly})_2]^{21-}$ (Ln = Gd^{3+} , Tb^{3+} , Dy^{3+} , Ho^{3+} , Y^{3+}) ^{6c}	$\text{K}_{14}[\text{As}_2\text{W}_{19}\text{O}_{67}(\text{H}_2\text{O})]/\text{Ln}(\text{NO}_3)_3\cdot 6\text{H}_2\text{O}/\text{gly}/\text{DABCO}$	5.7	aqueous method
2011	$\text{K}_{1.3}\text{Na}_3.2\text{H}_{6.5}[\text{L-Pr}(\text{PW}_{11}\text{O}_{39})_2]\cdot 8.3\text{L-proline}\cdot 21.5\text{H}_2\text{O}$ ^{6f} $\text{K}_{1.3}\text{Na}_3.2\text{H}_{6.5}[\text{D-Pr}(\text{PW}_{11}\text{O}_{39})_2]\cdot 8.3\text{D-proline}\cdot 17\text{H}_2\text{O}$ $\text{K}_{1.3}\text{Na}_3.2\text{H}_{6.5}[\text{L-Er}(\text{PW}_{11}\text{O}_{39})_2]\cdot 8.3\text{L-proline}\cdot 22.5\text{H}_2\text{O}$	$\text{Na}_9[\text{A-}\alpha\text{-PW}_9\text{O}_{34}]\cdot 16\text{H}_2\text{O}/\text{Ln}(\text{NO}_3)_3\cdot 6\text{H}_2\text{O}/\text{L- or D-proline}$	1.5	aqueous method
2013	$[\text{Ln}_6(\text{H}_2\text{O})_8]\{\text{As}_4\text{W}_{44}(\text{OH})_2(\text{proline})_2\text{O}_{151}\}^{10-}$ (Ln = Tb^{3+} , Dy^{3+} , Nd^{3+}) ^{6b}	$\text{K}_{14}[\text{As}_2\text{W}_{19}\text{O}_{67}(\text{H}_2\text{O})]/\text{Ln}(\text{NO}_3)_3\cdot 6\text{H}_2\text{O}/\text{L-proline}$	1.5	aqueous method
2014	$[\text{As}^{\text{III}}_4(\text{Y}^{\text{III}}\text{W}^{\text{VI}}_3)\text{W}^{\text{VI}}_{44}\text{Y}^{\text{III}}_{159}(\text{gly})_8(\text{H}_2\text{O})_{14}]^{9-6d}$	$\text{K}_{14}[\text{As}_2\text{W}_{19}\text{O}_{67}(\text{H}_2\text{O})]/\text{gly}(\text{aq})/\text{Y}(\text{NO}_3)_3\cdot 6\text{H}_2\text{O}/\text{p-MeBzNH}_2$	2.0–2.2	aqueous method
2015	$\text{KNa}_3[\text{HPro}]_7[\text{Sm}(\alpha\text{-PW}_{11}\text{O}_{39})_2]\cdot \text{Pro}\cdot 18\text{H}_2\text{O}$ ^{6e}	$\text{Na}_9[\text{A-}\alpha\text{-PW}_9\text{O}_{34}]\cdot 7\text{H}_2\text{O}/\text{D-proline}/\text{SmCl}_3$	1.5	aqueous method

Bond valence sum (BVS) calculations of **1–6** manifest that the oxidation states of all W, Ln, B elements are +6, +3, and +3, respectively (Table S1). The phase purity of **1–6** is confirmed by the good consistency of the experimental PXRD patterns of the bulks with the simulated PXRD patterns from the single-crystal structural analyses (Fig. S2).

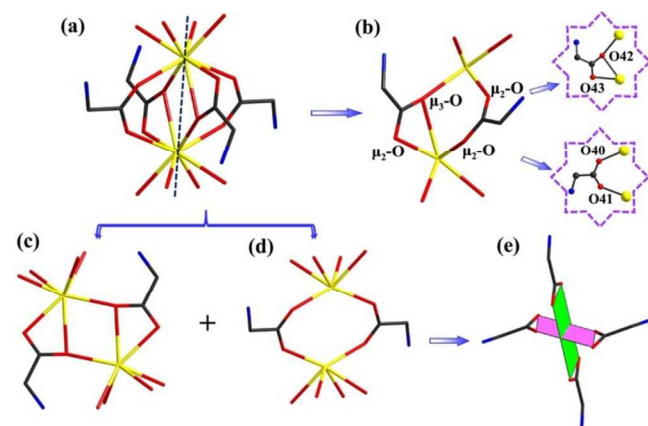


Fig. 2 (a) The $\{\text{Ce}_2(\text{gly})_4\}$ cluster in **1**. (b) The $\mu_2\text{-O}$ and $\mu_3\text{-O}$ atoms in $\{\text{Ce}_2(\text{gly})_4\}$ cluster. (c) and (d) The connection modes of gly ligands with the Ce^{3+} cations. (e) Two almost perpendicular planes respectively defined by four carboxylic O atoms in each of two types of gly ligands showing the dihedral angle of 85.0° .

1–6 are isostructural and belong to the monoclinic space group $P2(1)/c$, all of which possess a particular dimeric structure established by two mono-Ln substituted Keggin $[\text{Ln}(\alpha\text{-BW}_{11}\text{O}_{39})]^{6-}$ BT subunits bridged by four gly bridges. As far as we know, they stand for the first inorganic–organic hybrid LSBs functionalized by amino acid ligands. Therefore, only **1** is taken as an example to be discussed. The molecular structure of **1** consists of an inorganic–organic hybrid dumbbell-shaped $[\text{Ce}_2(\text{gly})_4(\text{BW}_{11}\text{O}_{39})_2]^{12-}$ polyoxoanion (Fig. 1a), four K^+ ions, four Na^+ ions, four H^+ ions and twenty-three lattice water molecules. It is noteworthy that the centric dumbbell-shaped $[\text{Ce}_2(\text{gly})_4(\alpha\text{-BW}_{11}\text{O}_{39})_2]^{12-}$ polyoxoanion can be described as the combination of two identical symmetrically related $[\text{Ce}(\alpha\text{-BW}_{11}\text{O}_{39})]^{6-}$ fragments (Fig. 1b) via four gly linkages (Fig. 1c). Two mono-Ln substituted Keggin $[\text{Ce}(\alpha\text{-BW}_{11}\text{O}_{39})]^{6-}$ symmetrically related fragments display the head-to-head fashion. In the $[\alpha\text{-BW}_{11}\text{O}_{39}]^{9-}$ fragment, the central B atom is surrounded by three $\mu_4\text{-O}$ atoms from three vertex-sharing $\{\text{W}_3\text{O}_{13}\}$ triads and one $\mu_3\text{-O}$ atom from an edging-sharing $\{\text{W}_2\text{O}_{10}\}$ dimer with the B–O distances of $1.50(2)$ – $1.53(2)$ Å and the O–B–O bond angles of $104.4(14)$ – $113.6(15)^\circ$, leading to a distorted tetrahedral geometry. In **1**, there is one crystallographically unique Ce^{3+} cation that binds to four terminal O atoms (O18, O21, O30, O38) from one $[\alpha\text{-BW}_{11}\text{O}_{39}]^{9-}$ subunit [Ce–O: $2.481(13)$ – $2.523(14)$ Å] and five carboxyl O atoms (O40A, O41, O42, O42A, O43A) [Ce–O: $2.482(14)$ – $2.774(14)$ Å] from four gly ligands achieving a nona-coordinate severely distorted monocapped square antiprismatic geometry (Fig. 1d), in which two bottom planes are respectively occupied by O18, O21, O30, O38 group and O40A, O41, O42, O43A group while the cap position is situated by O42A. The Ce–O bond lengths of $2.481(13)$ – $2.774(14)$ Å

and the O–Ce–O bond angles of $48.8(4)$ – $144.4(5)^\circ$ are basically within the normal range for nona-coordinate Ce^{3+} system.¹⁴ There are two crystallographically independent gly molecules, which adopt the didentate coordination fashion and coordinate to two Ce^{3+} cations through carboxylic O atoms with the Ce···Ce distance of $4.124(16)$ Å (Fig. 2a). It is very fascinating that their binding modes are somewhat different although two gly ligands utilize the didentate coordination fashion, in which both carboxylic O atoms (O40, O41) from the first-type gly ligand display the same $\mu_2\text{-O}$ pattern while two carboxylic O atoms (O42, O43) from the second-type gly ligand show the $\mu_2\text{-O}$ and $\mu_3\text{-O}$ patterns (Fig. 2b–d). More interestingly, two planes respectively defined by four carboxylic O atoms in each of two types of gly ligands are almost perpendicular to each other with the dihedral angle of $85.047(7)^\circ$ (Fig. 2e) and this distribution mode is beneficial to enhance the structural stability of **1**. As far as we are aware, this distribution mode was first encountered among LSPs functionalized by amino acid ligands, delegating a rare example of amino acid inclusion within a POT polyoxoanion in contrast to those containing coordination of gly, ala, or pro ligands via carboxylic O atoms in a $\mu_2\text{-O}$ bridging binding mode to Ln^{3+} cations or W metal centers, or even both of them.^{36–40}

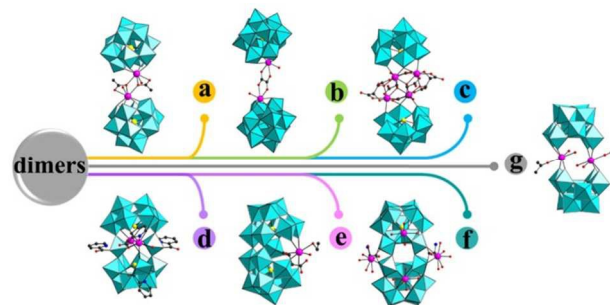
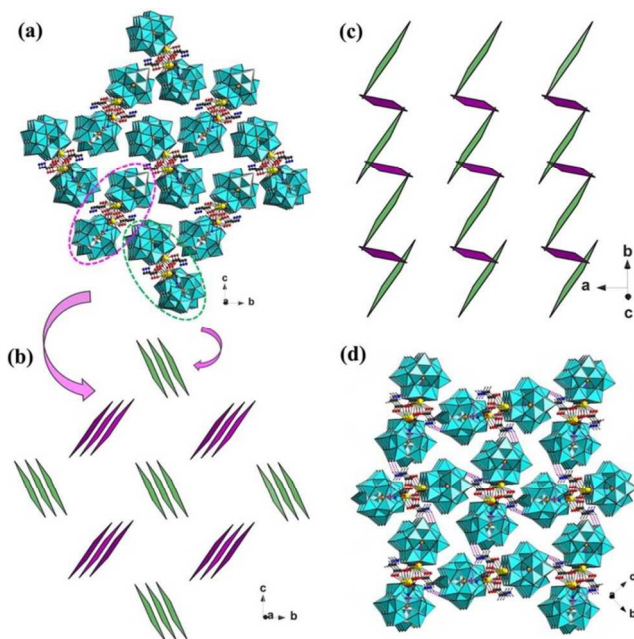


Fig. 3 Some representative inorganic–organic hybrid dimeric LSPs.

Notably, some inorganic–organic hybrid dimeric LSPs derived from the fusion of two lacunary Keggin-type POT fragments have been addressed (Fig. 3), in which the coordination water molecules grafting to the Ln^{3+} cations can be partially or totally substituted by organic ingredients. One common structure type is that two Ln-substituted POT fragments are connected by organic linkages, giving rise to the sandwich-type dimeric LSPs such as the mono-carboxylate bridging complexes $[\{\text{Ln}(\alpha\text{-XW}_{11}\text{O}_{39})(\text{H}_2\text{O})_2\}_2(\mu\text{-CH}_3\text{COO})_2]^{10/12-}$ ($\text{X} = \text{P}^{\text{V}}, \text{Si}^{\text{IV}}$) (Fig. 3a)^{5d–h}, di-carboxylate bridging species $[\{\alpha\text{-PW}_{11}\text{O}_{39}\}\text{Ln}(\text{H}_2\text{O})_2(\text{C}_2\text{O}_4)\}_2]^{10-}$ (Fig. 3b) and $[\text{Ln}_2(\text{C}_4\text{H}_4\text{O}_6)(\text{C}_4\text{H}_2\text{O}_6)(\text{AsW}_9\text{O}_{33})_2]^{18-}$ (Fig. 3c),^{5m,5r} in which organic components not only participate in the substitution reaction of water ligands but also play an important bridging role on the assembly of dimeric polyoxoanions. The other structure type is related to those dimers decorated by organic ligands such as W-linked complex $[\text{Tb}_2(\text{pic})(\text{H}_2\text{O})_2(\text{B-}\beta\text{-AsW}_8\text{O}_{30})_2(\text{WO}_2(\text{pic}))_3]^{10-}$ (Fig. 3d),^{5l} the chiral tartrate-based POT $[\text{Ce}(\text{H}_2\text{O})(\text{CH}_3\text{CH}_2\text{OH})(\text{L/D-tartH}_3)(\text{Si}_2\text{W}_{10}\text{O}_{66})]^{8-}$ (Fig. 3e),^{5s} and the gly-encapsulated polyoxoanion $[\text{Dy}_4\text{As}_2\text{W}_{22}\text{O}_{76}(\text{H}_2\text{O})_{19}(\text{C}_2\text{H}_5\text{NO}_2)_2]^{2-}$ (Fig. 3f).^{6c} Furthermore, the water ligands replaced by organic solvent molecules were also observed in $[\{\text{Ln}(\text{H}_2\text{O})_2(\text{acetone})\}_2(\gamma\text{-SiW}_{10}\text{O}_{36})_2]^{10-}$ ($\text{Ln} = \text{Y}^{3+}, \text{Nd}^{3+}, \text{Eu}^{3+}, \text{Gd}^{3+}, \text{Tb}^{3+}, \text{Dy}^{3+}$) (Fig. 3g).¹⁵ In contrast, the feature that four gly molecules

coordinating to a Ce^{3+} ion incorporated in the lacunary pocket of the $[\alpha\text{-BW}_{11}\text{O}_{39}]^{9-}$ skeleton in **1** makes **1** outstanding among the previously reported dimeric LSPs, and thus **1** represents the first inorganic–organic hybrid gly-functionalized LSBs.

5 Additionally, free $[\text{Ce}_2(\text{gly})_4(\alpha\text{-BW}_{11}\text{O}_{39})_2]^{12-}$ units are regularly distributed in the arrangement mode of –ABA– (Fig. 4a). A closer examination reveals that neighboring $[\text{Ce}_2(\text{gly})_4(\alpha\text{-BW}_{11}\text{O}_{39})_2]^{12-}$ units are oppositely aligned in a staggered fashion (Fig. 4b, c), which could effectively reduce the steric hindrance and favors the closest
10 packing of $[\text{Ce}_2(\text{gly})_4(\alpha\text{-BW}_{11}\text{O}_{39})_2]^{12-}$ units. It is worth noting that the incorporation of Ln^{3+} cations into POMs is an important topic in the field of supramolecular chemistry, in which the building blocks formed by Ln^{3+} cations and POMs can be interconnected through hydrogen bonds or van der Waals interactions to generate 3-D
15 supramolecular framework and these POM-based supramolecular complexes are one promising candidate in the domain of chemobiology, material chemistry, etc. From the view of supramolecular chemistry, the 3-D supramolecular architecture also exists in **1** taking into consideration the H-bonding interactions
20 between the N atoms of gly ligands and the surface O atoms of the BT units and water molecules (Fig. 4d, S3). For each gly molecule, only one N atom participates into the formation of N–H \cdots O interactions as O atoms are totally involved in the coordination with Ln^{3+} cations. Consequently, the combined interactions between the
25 proton donors served by gly ligands and proton acceptors coming from the surface O atoms of the BT units as well as water molecules lead to the infinitely 3-D supramolecular structure with the N–H \cdots O distances in the range of 2.83(3)–3.34(3) Å.



30 **Fig. 4** (a) The 3-D packing of discrete $[\text{Ce}_2(\text{gly})_4(\alpha\text{-BW}_{11}\text{O}_{39})_2]^{12-}$ units. (b) and (c) The simplified 3-D packing modes in two different directions. (d) The 3-D supramolecular architecture of **1**. Pink bonds highlight the hydrogen-bonding interactions.

Another arresting structural characteristic of **1** is that the dimeric
35 $[\text{Ce}_2(\text{gly})_4(\alpha\text{-BW}_{11}\text{O}_{39})_2]^{12-}$ units are cemented by bridging K^+ and

Na^+ ions propagating the beautiful 3-D architecture (Fig. 5a, S4). It is exciting to find that two $\{\text{K}_2\text{Na}_2\}$ clusters like two arms are situated at both sides of the central $\{\text{Ce}_2(\text{gly})_4\}$ unit (Fig. 5b, S5) to “shake hands” with neighboring $\{\text{BW}_{11}\text{O}_{39}\}$ fragments and
40 accomplish the assembly of the 3-D structure. As far as we are aware, alkali metal cations such as K^+ or Na^+ ions originating from the starting materials or additional alkali metal salts play an important role in the assembly of final products in the POT chemistry. Generally speaking, the functionalities of alkali metal cations can be
45 summarized into three aspects except the common role of charge compensation: (i) The regulating effect: in 2006, Gutiérrez-Zorrilla et al. discovered that when Na^+ , K^+ , Rb^+ acetate buffers are respectively used, three different silicotungstates $\text{K}_8[\text{Si}_2\text{W}_{22}\text{Cu}_2\text{O}_{78}(\text{H}_2\text{O})]$, $\{\text{Cu}_2(\text{ac})_2(\text{phen})_2(\text{H}_2\text{O})\}_2 \cdot \sim 40\text{H}_2\text{O}$, $\text{K}_4[\text{SiW}_{11}\text{O}_{39}\text{Cu}(\text{H}_2\text{O})]$, $\{\text{Cu}_2(\text{ac})_2(\text{phen})_2(\text{H}_2\text{O})\}_2 \cdot 14\text{H}_2\text{O}$ and $\text{Cs}_7[\text{Cu}_2(\text{ac})_2(\text{phen})_2(\text{H}_2\text{O})_2][\text{Cu}_3(\text{ac})_3(\text{phen})_3(\text{H}_2\text{O})_3]$
50 $[\text{Si}_2\text{W}_{22}\text{Cu}_2\text{O}_{78}(\text{H}_2\text{O})] \cdot \sim 18\text{H}_2\text{O}$ (ac = acetate, phen = 1,10-phenanthroline) were obtained, indicating that the structures of the outcomes highly depend on the size of alkaline cations.¹⁶ Afterwards, Zhao et al. further confirmed this viewpoint.¹⁷ (ii) The template effect:
55 in this respect, K^+ ion is encapsulated in the cavity and plays a key role in the formation and stabilization of the whole structure,¹⁸ such as the unprecedented crown-shape species $[\text{K} \subset \text{K}_7\text{Ce}_{24}\text{Ge}_{12}\text{W}_{120}\text{O}_{456}(\text{OH})_{12}(\text{H}_2\text{O})_{64}]^{52-}$ that can be regarded as the outcome of the K^+ -directed self-assembly of twelve $[\text{Ce}_2\text{GeW}_{10}\text{O}_{38}]^{6-}$ units.^{18a} (iii) The
60 bridging effect: alkali metal cations usually have a high affinity for the POT anions as well as solvent molecules and are liable to associate with terminal O groups of the polyoxoanions to produce $[\text{M}(\text{H}_2\text{O})_n]^+$ units, conducive to the construction of polymeric or high-dimensional POTs.¹⁹

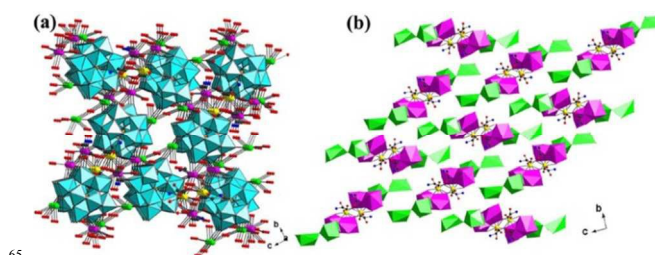


Fig. 5 (a) The 3-D architecture constructed from the K^+ and Na^+ cations in **1**. (b) The regular alignment of the $\{\text{K}_4\text{Na}_4\text{Ce}_2(\text{gly})_4\}$ cluster in the 3-D structure of **1**. $\{\text{KO}_8\}$: pink; $\{\text{NaO}_6\}$ and $\{\text{NaO}_7\}$: bright green.

IR spectra

70 The IR spectra of **1–6** have been recorded in the range of 4000–400 cm^{-1} from solid samples palletized with KBr, which are presented in Fig. S1. It is obviously seen that all of them have similar four characteristic vibration patterns in the low wavenumber scope ($\nu < 1000 \text{ cm}^{-1}$), corresponding to the analogous basic BT fragments in their skeletons. The four characteristic peaks at 948, 877, 822 and 691 cm^{-1} for **1**, 947, 878, 819 and 691 cm^{-1} for **2**, 946, 874, 819 and 697 cm^{-1} for **3**, 948, 877, 826 and 702 cm^{-1} for **4**, 946, 875, 821 and 697 cm^{-1} for **5**, 947, 878, 826 and 700 cm^{-1} for **6** are respectively ascribed to terminal $\nu(\text{W}-\text{O}_t)$, $\nu(\text{B}-\text{O})$, corner-sharing $\nu(\text{W}-\text{O}_b)$ and
75 edge-sharing $\nu(\text{W}-\text{O}_c)$ of the $[\alpha\text{-BW}_{11}\text{O}_{39}]^{9-}$ polyoxoanion. Compared to $\text{K}_8[\alpha\text{-BW}_{11}\text{O}_{39}\text{H}] \cdot 13\text{H}_2\text{O}$ [954, 886, 837 and 745 cm^{-1} for $\nu(\text{W}-\text{O}_t)$, $\nu(\text{B}-\text{O})$, $\nu(\text{W}-\text{O}_b)$ and $\nu(\text{W}-\text{O}_c)$], the shifts of $\nu(\text{W}-\text{O}_t)$,

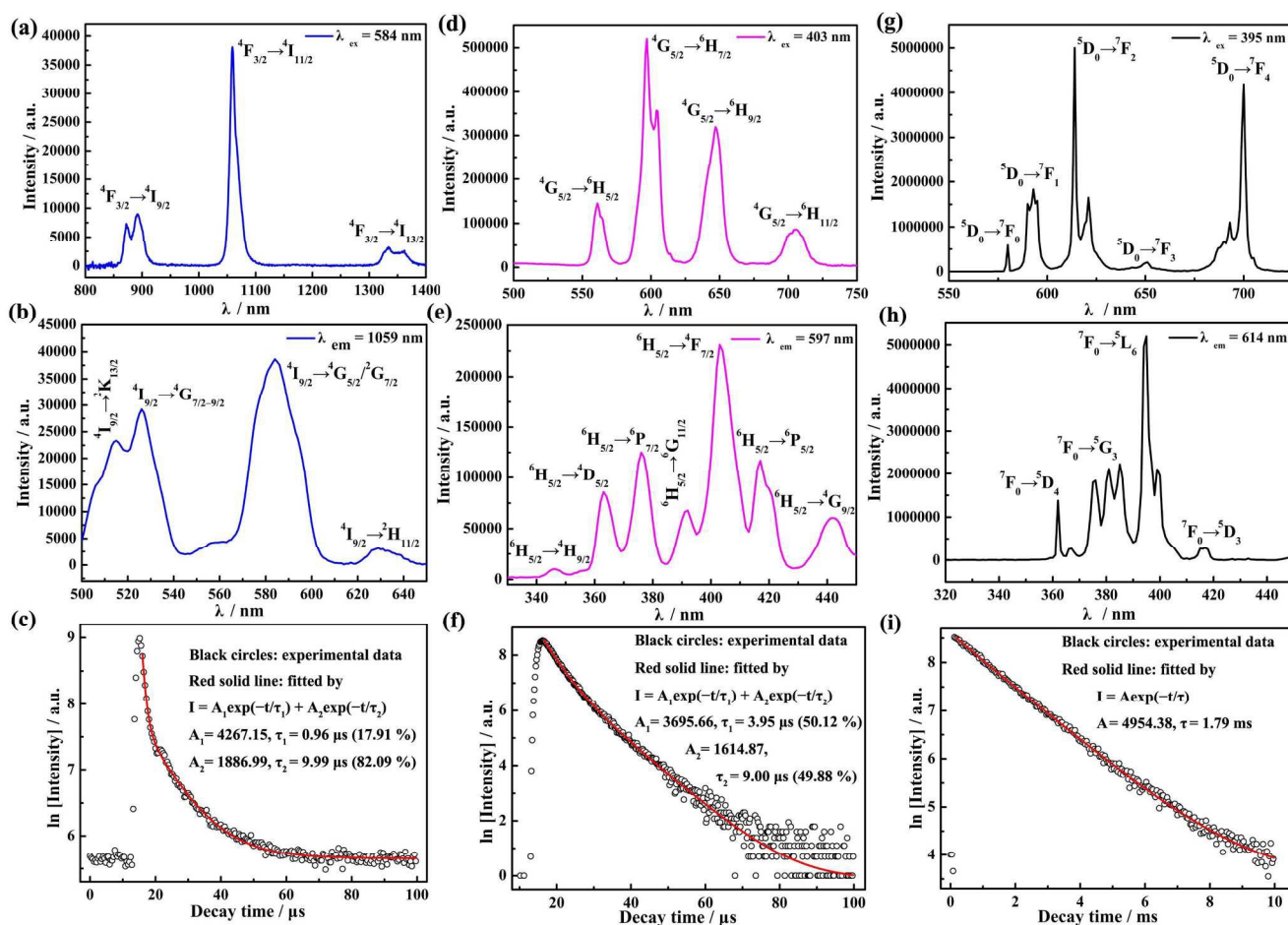


Fig. 6 (a) The solid-state emission spectrum of **3** ($\lambda_{\text{ex}} = 584$ nm) at room temperature. (b) The solid-state excitation spectrum of **3** ($\lambda_{\text{em}} = 1059$ nm) at room temperature. (c) The luminescence decay curve of **3** taken by monitoring the emission at 1059 nm with τ_1 and τ_2 as 0.96 μs (17.91 %) and 9.99 μs (82.09 %). (d) The solid-state emission spectrum of **4** ($\lambda_{\text{ex}} = 403$ nm) at room temperature. (e) The solid-state excitation spectrum of **4** ($\lambda_{\text{em}} = 597$ nm) at room temperature. (f) The luminescence decay curve of **4** taken by monitoring the emission at 597 nm with τ_1 and τ_2 as 3.95 μs (17.91 %) and 9.00 μs (82.09 %). (g) The solid-state emission spectrum of **5** ($\lambda_{\text{ex}} = 395$ nm) at room temperature. (h) The solid-state excitation spectrum of **5** ($\lambda_{\text{em}} = 614$ nm) at room temperature. (i) The luminescence decay curve of **5** taken by monitoring the emission at 614 nm with τ as 1.97 ms.

$\nu(\text{B}-\text{O})$, $\nu(\text{W}-\text{O}_\text{b})$ and $\nu(\text{W}-\text{O}_\text{c})$ are related to the implantation of the Ln^{3+} cation to the defect site of the $[\alpha\text{-BW}_{11}\text{O}_{39}]^{9-}$ segment, leading to the deformation and distortion of the $[\alpha\text{-BW}_{11}\text{O}_{39}]^{9-}$ skeleton. In the high wavenumber region ($\nu > 1000$ cm^{-1}), an intense and broad absorption band at 3394–3442 cm^{-1} as well as a strong absorption band at 1621–1645 cm^{-1} are observed, which are ascribed to the stretching and bending vibration modes of water molecules, respectively. It should be noted that there is some overlap between the $\nu(\text{C}=\text{O})$ absorption band of gly ligands and the intense bending vibration band of water molecules. In the IR spectrum of the free gly ligand, the asymmetric and symmetric vibrations of the carboxylate group are seen at 1621 cm^{-1} and 1413 cm^{-1} . Compared with the free gly ligand, the appearance of weak peaks derived from asymmetric and symmetric vibrations of the carboxylate group of the gly ligand in the IR spectra of **1–6** is indicative of the presence of gly components in **1–6**. Specifically, the resonances at 1624–1640 cm^{-1} and 1412–1416 cm^{-1} are discriminably attributed to the asymmetric stretching vibration and symmetric stretching vibration of the carboxylate groups [named as $\nu_{\text{as}}(\text{COO})$ and $\nu_{\text{s}}(\text{COO})$, respectively], which have some shifts to some extent in contrast to the free gly

ligand, suggesting that gly ligand coordinates to the Ln^{3+} cations. Generally speaking, the difference ($\Delta\nu$) between the $\nu_{\text{as}}(\text{COO})$ and $\nu_{\text{s}}(\text{COO})$ is often applied as a criterion to evaluate the coordination mode of the carboxylate group.^{5k,20} Herein, the $\Delta\nu$ of 212–224 cm^{-1} in **1–6** demonstrates that the gly ligands in **1–6** employ the bridging coordination mode, which is in good agreement with the results of X-ray single-crystal diffraction. In addition, the peak located at 1339–1343 cm^{-1} is assigned to the $\nu(\text{C}-\text{N})$ vibration, while the $\text{Ln}-\text{O}$ stretching vibrations of **1–6** are absent in the IR region probably resulting from the prominent ionic interactions between the lacunary POT segments and Ln^{3+} cations.^{5d}

Photoluminescence (PL) properties

The PL properties of Ln^{3+} ions have been fascinating researchers for several decades and evoked great interest in the biomedical analyses, cathode ray tubes, light-emitting diodes, fluorescent tubes and efficient light conversion molecular devices due to their particular luminescence features such as high luminescence quantum yield, narrow bandwidth, long-lived emission and large Stokes shift.²¹ As is well known, Eu^{3+} and Tb^{3+} complexes are the most intense emitters

that respectively emit red and green light among the Ln series, and are widely used as luminescence materials for easily detected emissions in the visible region while Nd^{3+} , Er^{3+} , and Yb^{3+} complexes are applied in biological analysis for the sake of their almost transparent near-infrared (NIR) emissions in biological issues.²² These unique functionalities are assigned to the transitions inside the 4f shell of Ln^{3+} ions involving in the shielding of the partially filled 4f orbits by the closed 5s² and 5p⁶ shells resulting in the characteristic narrow line-like emissions²³ and the long lifetimes of the excited states. In this paper, the luminescent properties and lifetime decay behaviors of **3**, **4** and **5** in the solid state were investigated at ambient temperature.

When **3** is excited at 584 nm, its NIR PL emission spectrum (Fig. 6a) displays three characteristic emission bands, which are assigned to $^4\text{F}_{3/2} \rightarrow ^4\text{I}_{9/2}$ (870 and 892 nm), $^4\text{F}_{3/2} \rightarrow ^4\text{I}_{11/2}$ (1059 nm) and $^4\text{F}_{3/2} \rightarrow ^4\text{I}_{13/2}$ (1334 nm) transitions of Nd^{3+} ions, respectively.²⁴ In terms of Nd^{3+} excitation, some transitions to different states are not resolved and the excitation bands are relatively broad on account of the multiplicity of excited 4f states in the visible region. Hence, several bands were apperceived in the excitation spectrum monitored at $^4\text{F}_{3/2} \rightarrow ^4\text{I}_{11/2}$ transition at 1059 nm for **3**, corresponding to the Nd^{3+} f-f transitions located at 515 nm ($^4\text{I}_{9/2} \rightarrow ^2\text{K}_{13/2}$), 526 nm ($^4\text{I}_{9/2} \rightarrow ^4\text{G}_{7/2}/^4\text{G}_{9/2}$), 584 nm ($^4\text{I}_{9/2} \rightarrow ^4\text{G}_{5/2}/^2\text{G}_{7/2}$), 628 nm ($^4\text{I}_{9/2} \rightarrow ^2\text{H}_{11/2}$) (Fig. 6a). In order to determine the lifetime, the luminescent decay curve of **3** (Fig. 6c) by monitoring at the strongest emission of $^4\text{F}_{3/2} \rightarrow ^4\text{I}_{11/2}$ was carried out, which can be fitted to a double exponential function $I = A_1\exp(-t/\tau_1) + A_2\exp(-t/\tau_2)$ (where τ_1 and τ_2 are the fast and slow components of the luminescence lifetimes; A_1 and A_2 are the pre-exponential factors), affording the luminescent lifetimes τ_1 and τ_2 as 0.96 μs (17.91 %) and 9.99 μs (82.09 %), and the agreement factors (χ^2) of 1.296, respectively. The average lifetime (τ) of **3** is 8.38 μs based on the formula $\tau = [A_1\tau_1^2 + A_2\tau_2^2]/[A_1\tau_1 + A_2\tau_2]$ (Table S2).²⁵ Theoretically, the lifetime decay of **3** should abide by a single exponential function since there is only one crystallographically unique Nd^{3+} ion in the structure. To gain insight into the origin of two lifetimes of **3**, the luminescence emission of the precursor $\text{K}_8[\alpha\text{-BW}_{11}\text{O}_{39}\text{H}]\cdot 13\text{H}_2\text{O}$ was performed under the similar conditions to **3**. Unfortunately, $\text{K}_8[\alpha\text{-BW}_{11}\text{O}_{39}\text{H}]\cdot 13\text{H}_2\text{O}$ does not exhibit any luminescence emission in the NIR region (Fig. S6). As a consequence, it can be inferred that the di-exponential decay behavior of **3** may be attributed to the interactions between Nd^{3+} centers (the $\text{Nd}^{3+}\cdots\text{Nd}^{3+}$ distance is 4.1152(2) Å, which comes from the result of X-ray single-crystal diffraction).

The solid-state PL emission spectrum of **4** (Fig. 6d) under excitation at 403 nm was measured at room temperature, giving birth to the pink emission of Sm^{3+} ion originating from the $^4\text{G}_{5/2}$ level appearing at 561, 597, 605, 648, and 705 nm, respectively. The strongest emission peaks located at 597 nm with a splitting peak around 605 nm are derived from the $^4\text{G}_{5/2} \rightarrow ^6\text{H}_{7/2}$ transition of Sm^{3+} while the peaks centered at 561, 648 and 705 nm are severally attributed to $^4\text{G}_{5/2} \rightarrow ^6\text{H}_{5/2}$, $^4\text{G}_{5/2} \rightarrow ^6\text{H}_{9/2}$ and $^4\text{G}_{5/2} \rightarrow ^6\text{H}_{11/2}$, respectively.²⁶ The excitation spectrum of **4** (Fig. 6e) detected at the Sm^{3+} $^4\text{G}_{5/2} \rightarrow ^6\text{H}_{7/2}$ transition (597 nm) is dominated by the $^6\text{H}_{5/2} \rightarrow ^4\text{F}_{7/2}$ transition at 403 nm, whereas the observable weaker peaks can be assigned to the transitions from the $^6\text{H}_{5/2}$ ground state to the $^4\text{H}_{9/2}$ at 346 nm, $^4\text{D}_{5/2}$ at 363 nm, $^6\text{P}_{7/2}$ at 376 nm, $^6\text{G}_{11/2}$ at 391 nm, $^6\text{P}_{5/2}$ at 417 nm and $^4\text{G}_{9/2}$ at 441 nm, respectively.²⁶ The lifetime decay curve for $^4\text{G}_{5/2}$ level of **4** (Fig. 6f) under excitation at 403 nm and emission

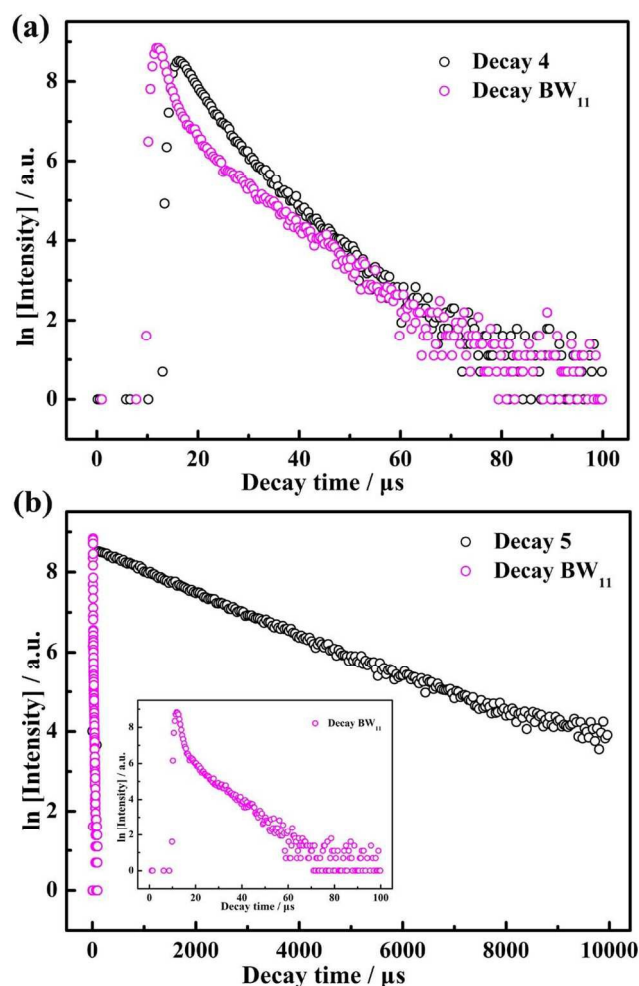


Fig. 7 (a) The luminescence decay curves of **4** and $\text{K}_8[\alpha\text{-BW}_{11}\text{O}_{39}\text{H}]\cdot 13\text{H}_2\text{O}$ (BW_{11}) taken by monitoring the emission at 597 nm. (b) The luminescence decay curves of **5** and BW_{11} taken by monitoring the emission at 614 nm. Insert: an enlarged view of the decay curve of BW_{11} .

at 597 nm can be fitted to a double exponential function generating the lifetime values τ_1 and τ_2 of 3.95 μs (50.12 %) and 9.00 μs (49.88 %) with the average lifetime of 6.47 μs and the agreement factor (χ^2) of 1.073. Under similar conditions, the luminescence emission spectrum and the lifetime decay curve of the precursor $\text{K}_8[\alpha\text{-BW}_{11}\text{O}_{39}\text{H}]\cdot 13\text{H}_2\text{O}$ were examined under emission at 597 nm and excitation at 403 nm. The emission spectrum of $\text{K}_8[\alpha\text{-BW}_{11}\text{O}_{39}\text{H}]\cdot 13\text{H}_2\text{O}$ reveals a broad band at around 700 nm (Fig. S7), the intensity of which is relatively weak so that it was overlapped by the typical peak $^4\text{G}_{5/2} \rightarrow ^6\text{H}_{11/2}$ of **4** at 705 nm, suggesting that the energy transfer from the $[\alpha\text{-BW}_{11}\text{O}_{39}]^{9-}$ fragments to Sm^{3+} centers may happen. This result is further confirmed by the bi-exponential decay curve of $\text{K}_8[\alpha\text{-BW}_{11}\text{O}_{39}\text{H}]\cdot 13\text{H}_2\text{O}$ with $\tau_1 = 1.68 \mu\text{s}$ (42.21 %) and $\tau_2 = 9.31 \mu\text{s}$ (57.79 %) (Fig. S8). The average lifetime is calculated to be 6.09 μs , approximately to that of **4** (Fig. 7a), thus it can be reasonably assessed that the $[\alpha\text{-BW}_{11}\text{O}_{39}]^{9-}$ fragments make some of the contribution to the PL behavior of **4** by the energy transfer of the O \rightarrow W transitions to Sm^{3+} centers during the emission process of **4**. As an important parameter to characterize the efficiency

of the emission process, the luminescence quantum yields (Φ) of **4** and $\text{K}_8[\alpha\text{-BW}_{11}\text{O}_{39}\text{H}]\cdot 13\text{H}_2\text{O}$ were determined using an integrating sphere at ambient temperature under excitation at 403 nm, and the emission quantum yields are found to be 7.45 % (Fig. S9) and 5.98 % (Fig. S10), respectively. The relatively approximate Φ values further confirm the energy transfer from $\text{K}_8[\alpha\text{-BW}_{11}\text{O}_{39}\text{H}]\cdot 13\text{H}_2\text{O}$ to **4** in the emission procedure.

The emission spectrum of **5** (Fig. 6g) was measured under a maximum excitation at 395 nm, which exhibits the characteristic luminescent bands of Eu^{3+} ion centered at 580, 593, 614, 651 and 700 nm, attributed to the $^5\text{D}_0 \rightarrow ^7\text{F}_j$ ($j = 0-4$) transitions, respectively. The $^5\text{D}_0 \rightarrow ^7\text{F}_{1,3}$ transitions are magnetic-dipolar transitions that are insensitive to their local environments whereas the $^5\text{D}_0 \rightarrow ^7\text{F}_{0,2,4}$ transitions are electro-dipolar transitions that are fairly hypersensitive to their local environments.²⁷ As we know, the $^5\text{D}_0 \rightarrow ^7\text{F}_0$ emission is severely forbidden in a symmetric field, but the appearance of this symmetric forbidden transition at 580 nm in **5** suggests that the Eu^{3+} ions are situated in the lower symmetric ligand field. Moreover, the $^5\text{D}_0 \rightarrow ^7\text{F}_0$ transition just exhibits a single peak, from which we can also draw a conclusion on the low symmetry site of the Eu^{3+} ion in good agreement with the monocapped square antiprismatic geometry. The medium-strong emission at 593 nm is ascribed to the magnetic-dipole transition from $^5\text{D}_0 \rightarrow ^7\text{F}_1$ and its emission intensity barely varies with the strength of the ligand field acting on the Eu^{3+} ion. In contrast, the most intense emission at 614 nm assigned to the electro-dipolar transition from $^5\text{D}_0 \rightarrow ^7\text{F}_2$ transition is highly sensitive to the coordination environment of the Eu^{3+} ion and implies a red emission light. Generally speaking, the Eu^{3+} ion can be regarded as an excellent structure probe for investigation on the local environment in a host matrix on the basis of Judd-Ofelt theory.²⁸ If the Eu^{3+} ion is located in a centrosymmetric environment, the $^5\text{D}_0 \rightarrow ^7\text{F}_1$ transition should be dominant and in a noncentrosymmetric situation, the $^5\text{D}_0 \rightarrow ^7\text{F}_2$ transition would be the preponderant one.²⁹ As depicted in Fig. 6g, the intensity of $^5\text{D}_0 \rightarrow ^7\text{F}_{2,4}$ transitions are much stronger than that of $^5\text{D}_0 \rightarrow ^7\text{F}_{1,3}$, testifying that the Eu^{3+} ion doesn't reside in the inversion symmetric environment. Besides, the intensity of the $^5\text{D}_0 \rightarrow ^7\text{F}_2$ transition increases as the site symmetry of the Eu^{3+} center decreases. Thus, the intensity ratio of $I(^5\text{D}_0 \rightarrow ^7\text{F}_2)/I(^5\text{D}_0 \rightarrow ^7\text{F}_1)$ is usually used as a criterion of the change on the nature of Eu^{3+} local surroundings as well as the site symmetry of the Eu^{3+} ion.³⁰ In this work, the intensity ratio is ca. 2.7, illustrating that the site environment of Eu^{3+} ion is asymmetric, being consistent with the results of the single-crystal X-ray analysis. These values are lower than those observed for the Eu^{3+} ions in $[\text{Eu}(\text{H}_2\text{O})_8]_2[\text{Fe}_4(\text{H}_2\text{O})_8(\text{thr})_2]$ [B- β -SbW₉O₃₃]₂·22H₂O (4.7),^{13a} $[\text{Eu}(\text{pqc})(\text{Hpqc})(\text{NO}_3)_2]_n$ (5.5)³¹ and $\text{Cs}_3\text{K}_4[(\text{Ge}_2\text{W}_{18}\text{Nb}_6\text{O}_{78})\text{Eu}(\text{H}_2\text{O})_4]\cdot 23\text{H}_2\text{O}$ (7.3)⁵⁸. A greater intensity ratio may be related to a more distorted local cation environment. The excitation spectrum collected by monitoring the emission at 614 nm is presented in Fig. 6h, and the most intense peak is located at 395 nm ($^7\text{F}_0 \rightarrow ^5\text{L}_6$) whereas other weak peaks are observed at 362 nm ($^7\text{F}_0 \rightarrow ^5\text{D}_4$), 374–385 nm ($^7\text{F}_0 \rightarrow ^5\text{G}_3$) and 416 nm ($^7\text{F}_0 \rightarrow ^5\text{D}_3$).²⁶ The lifetime of luminescence for **5** was carried out and it can be fitted with a single exponential function $I = A\exp(-t/\tau)$, yielding a lifetime τ of 1.79 ms (Fig. 6i). In contrast, the luminescence lifetimes of $[\text{Eu}(\text{H}_2\text{O})_8]_2[\text{Fe}_4(\text{H}_2\text{O})_8(\text{thr})_2]$ [B- β -SbW₉O₃₃]₂·22H₂O (0.097 ms)^{13a} in which the Eu^{3+} ion is surrounded by eight water molecules and $\text{Na}_{0.5}\text{Cs}_{4.5}[\text{Eu}(\alpha\text{-SiW}_{11}\text{O}_{39})(\text{H}_2\text{O})_2]\cdot 23\text{H}_2\text{O}$ (0.39 ms)³³ in which two coordinate O atoms of the Eu^{3+} ion is derived from two water ligands

are evidently shorter than that of **5**, mainly resulting from the enhancement of the radiationless deactivation of the $^5\text{D}_0$ state and partially luminescence quench by the coordinate water ligands.³⁴ It should be noted that the emission characteristics are largely dependent on the environment of a given Ln^{3+} ion, such as the nature of a POM ligand, the symmetry and coordination geometry of the Ln^{3+} centers as well as the number of aqua coligands. On one hand, the presence of aqua ligands can lead to quenching the Ln^{3+} emission and shorting the luminescence lifetimes by coupling with proximal OH oscillators,^{19c} thus a little shorter decay lifetimes of $[\text{Eu}(\text{H}_2\text{O})_8]_2[\text{Fe}_4(\text{H}_2\text{O})_8(\text{thr})_2]$ [B- β -SbW₉O₃₃]₂·22H₂O and $\text{Na}_{0.5}\text{Cs}_{4.5}[\text{Eu}(\alpha\text{-SiW}_{11}\text{O}_{39})(\text{H}_2\text{O})_2]\cdot 23\text{H}_2\text{O}$ can be expected. On the other hand, Ln^{3+} cations usually suffer from weak luminescence due to the weak absorption coefficient ($< 10 \text{ mol}^{-1}\cdot\text{L}\cdot\text{cm}^{-1}$) resulting from the spin- and parity-forbidden f-f transitions.³⁵ This drawback can be overcome by the so-called “antenna effect” that organic ligands containing O or N atoms with suitable chromophores and tailored coordinate sites are utilized as sensitizers and connectors to absorb light and transfer energy from the organic ligands to the Ln^{3+} ions by intramolecular energy transfer.³⁶ Thus, the longer decay time of **5** is probably because of the chelation of gly ligands with Eu^{3+} cation precluding the coordination of quenching species such as water molecules to Eu^{3+} centers thereby reducing the nonradiative decay processes. Moreover, the PL emission and lifetime decay curve of $\text{K}_8[\alpha\text{-BW}_{11}\text{O}_{39}\text{H}]\cdot 13\text{H}_2\text{O}$ were carried out under the same conditions. The wide emission band at 576 nm was also veiled (Fig. S11) whilst the lifetime decay curve of $\text{K}_8[\alpha\text{-BW}_{11}\text{O}_{39}\text{H}]\cdot 13\text{H}_2\text{O}$ follows a bi-exponential decay function with τ_1 and τ_2 of 1.08 μs (44.19 %) and 9.36 μs (55.81 %) (Fig. S12) and the average lifetime is calculated as 5.70 μs . In comparison with the decay lifetime of **5** (1.79 ms), the lifetime contribution of the $[\alpha\text{-BW}_{11}\text{O}_{39}]^{9-}$ fragments in **5** can be almost negligible (Fig. 7b). Besides, the solid-state measurements of the luminescence quantum yields of **5** and $\text{K}_8[\alpha\text{-BW}_{11}\text{O}_{39}\text{H}]\cdot 13\text{H}_2\text{O}$ under the strongest excitation at 395 nm are 38.45 % for **5** (Fig. S13) and 4.41 % for $\text{K}_8[\alpha\text{-BW}_{11}\text{O}_{39}\text{H}]\cdot 13\text{H}_2\text{O}$ (Fig. S14), which also demonstrates the weak contribution of $\text{K}_8[\alpha\text{-BW}_{11}\text{O}_{39}\text{H}]\cdot 13\text{H}_2\text{O}$ in the emission of **5**.

The CIE 1931 diagram offers a pervasive method for studying the possible colors through combining three basic colors (red, blue and green) together, and has been widely utilized to quantify the tunability of the emission wavelength and the change of the emission intensity, as a result, good knowledge of the trueness of color is significant in the realm of lighting and display devices.³⁷ In the CIE chromaticity diagram, the chromaticity coordinates x and y , where, roughly speaking, x represents the red-to-blue ratio and y represents the green-to-blue ratio, are meaningful to determine the exact emission color of the sample when the white light emission is situated at the center position with the standard chromaticity coordinates ($x = 0.33333$, $y = 0.33333$). Here, the CIE chromaticity coordinates of **4** (0.59872, 0.40057) and **5** (0.63983, 0.35981) that are converted from their corresponding emission spectra are presented in Fig. S15.

Magnetic properties

The last few years have witnessed a large renaissance in the study of Ln^{3+} complexes owing to their large inherent anisotropy and unique electronic configuration such as the large number of unpaired 4f

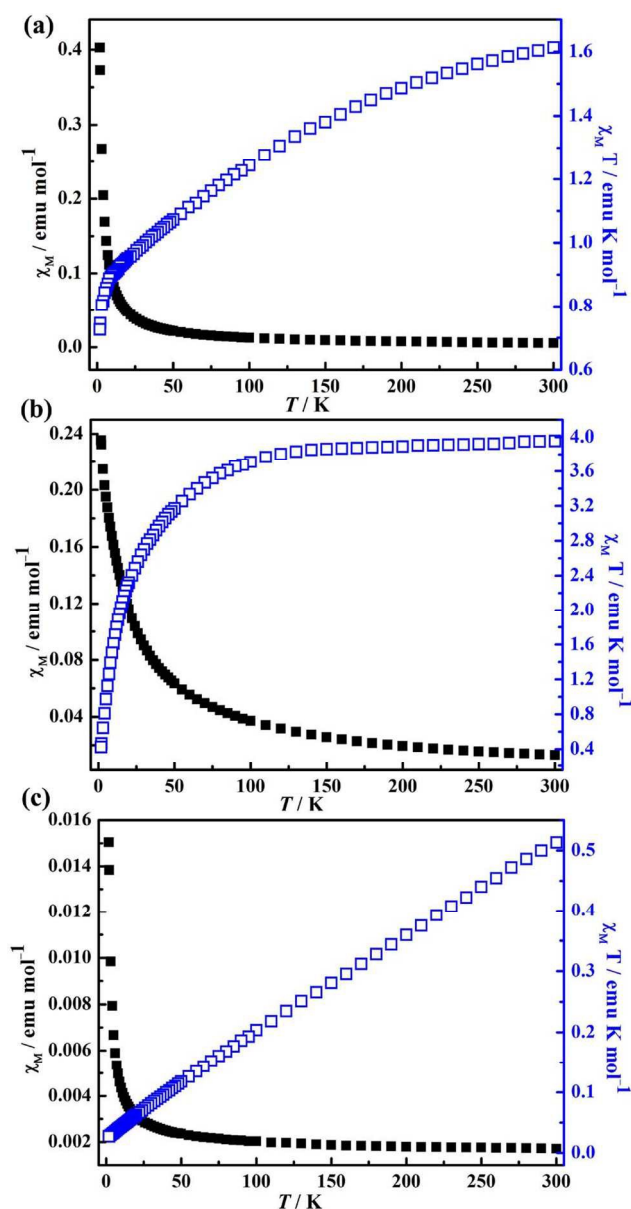


Fig. 8 Temperature dependence of the χ_M and $\chi_M T$ products at 1000 Oe for **1** (a), **2** (b) and **4** (c).

electrons. It is generally known that orbitally degenerate ground states of most Ln^{3+} ions, except for the isotropic Gd^{3+} ion with a $^8\text{S}_{7/2}$ single-ion ground state, are split by the spin-orbital coupling and crystal field effect.³⁸ Nevertheless, spin-orbital coupling interactions play a much more important role in the magnetic behaviors of Ln^{3+} cations compared with the small crystal field effect, as the large spin-orbital coupling can partly remove the degeneracy of the $4f^n$ group term of the $4f^n$ configuration for a Ln^{3+} cation, generating $2S+1L_J$ spectroscopic levels by the interelectronic repulsion and spin-orbit coupling, and each of these states is further split into Stark sublevels by the crystal field perturbation.^{38–39} As a consequence, the orbital contribution of the magnetic moment is more significant for Ln^{3+} cations.⁴⁰ Besides, the $2S+1L_J$ free-ground state for almost all the

Ln^{3+} cations is perfectly separated from the first excited state in energy so that only the ground state is thermally populated at ambient and low temperature.^{40–41} But when it comes to Eu^{3+} and Sm^{3+} , this situation is evidently different. The first excited state may be thermally populated owing to the small energy separation of 400 cm^{-1} for Eu^{3+} and 1000 cm^{-1} for Sm^{3+} ions, thus the possible crystal field effect as well as the thermal population of the higher energy state should be considered with regard to Eu^{3+} , or Sm^{3+} -containing POMs.³⁹ Along with the temperature decreasing, the effective magnetic moment of Ln^{3+} cations will alter by thermal depopulation of the Stark sublevels and the temperature dependence leads to the deviation of magnetic susceptibility from the Curie behavior.⁴²

Variable-temperature magnetic susceptibility measurements for **1**, **2** and **4** were preliminarily investigated in the temperature range of 1.8–300 K under a field of 1000 Oe. The plots of $\chi_M T$ vs. T and χ_M vs. T of **1**, **2** and **4** were displayed in Fig. 8. As for **1**, the $\chi_M T$ value at 300 K is 1.613 $\text{emu}^3 \text{K mol}^{-1}$, close to the theoretical value of 1.607 $\text{emu}^3 \text{K mol}^{-1}$ for two non-interacting Ce^{3+} ions ($S = 1/2$, $L = 3$, $g = 6/7$)⁴³ (Fig. 8a). Upon cooling, the $\chi_M T$ value decreases to a minimum of 0.725 $\text{emu}^3 \text{K mol}^{-1}$ at 1.8 K. This behavior can mainly be owing to the splitting of the 6-fold degenerate $^2F_{5/2}$ ground state affected by the crystal field perturbation and the progressive depopulation of the higher energy state upon cooling.^{5d,44} It is well-known that all the Stark levels split from the 6-fold degenerate $^2F_{5/2}$ ground state are equally populated at room temperature and with the temperature lowering, the Kramers doublets of higher energy are depopulated successively causing the decline of the $\chi_M T$ value with decreasing the temperature.⁴²

With respect to **2**, the room-temperature $\chi_M T$ value of 3.955 $\text{emu}^3 \text{K mol}^{-1}$ is slightly higher than the expected value of 3.20 $\text{emu}^3 \text{K mol}^{-1}$ for two non-interacting Pr^{3+} ions ($S = 1$, $L = 5$, $g = 4/5$) in the ground state (Fig. 8b). On the whole, the $\chi_M T$ value gradually decreases to reach a value of 0.424 $\text{emu}^3 \text{K mol}^{-1}$ as the temperature is lowered down to 1.8 K. For all we know, the 9-fold degenerate 3H_4 ground state of Pr^{3+} ions could be split into Stark levels by the crystal-field effect. As a result, the declining $\chi_M T$ value along with the decrease of temperature can be ascribed to the progressive population of the higher Stark levels for Pr^{3+} ions.⁴⁵

In the case of **4**, the experimental $\chi_M T$ value at 300 K is 0.513 $\text{emu}^3 \text{K mol}^{-1}$, slightly higher than expected value of 0.178 $\text{emu}^3 \text{K mol}^{-1}$ for two non-interacting Sm^{3+} ions ($^6H_{5/2}$, $J = 5/2$, $g = 2/7$),⁴⁶ as illuminated in Fig. 8c. As temperature descends, a linear decrease in $\chi_M T$ value is observed in the experimental data, maybe indicating the occurrence of antiferromagnetic couplings and the depopulation of the Kramers doublets of the higher energy of the Sm^{3+} . As is known, the $^6H_{5/2}$ ground-state term of the Sm^{3+} ion in the crystal field can be split into six levels ($J = 5/2, 7/2, 9/2, 11/2, 13/2, 15/2$), by spin-orbit coupling interactions, and the spin-orbit coupling parameter is 1200 cm^{-1} , therefore the crystal field effect and the possible thermal population of the high energy states should be considered for **4**.¹⁷ The minimum value of 0.027 $\text{emu}^3 \text{K mol}^{-1}$ at 1.8 K is much smaller than that of two non-interacting Sm^{3+} ions (0.178 $\text{emu}^3 \text{K mol}^{-1}$), demonstrating the presence of the comparatively stronger antiferromagnetic exchange interactions within the $\{\text{Sm}_2\}$ cluster mediated by the bridging carboxylic oxygen atoms from gly ligands as well as the spin-orbital coupling and the crystal field effect. Similar magnetic phenomenon has been encountered in the Sm^{3+} complex $\{\text{Na}[\text{Sm}(\text{pydc}(\text{OH})(\text{H}_2\text{O})_4)_3][\text{SiW}_{12}\text{O}_{40}]\cdot 15\text{H}_2\text{O}\}$.^{5t}

Conclusions

In conclusion, a series of novel organic–inorganic hybrid gly-bridging dimeric Keggin-type LSBs **1–6** have been prepared from the BT precursor and Ln^{3+} cations in the involvement of gly ligand by using an aqueous solution method, which represent the first LSBs functionalized by amino acid ingredients. The PL and lifetime decay behaviors of **3–5** and the magnetic properties of **1**, **2** and **4** have been studied. Furthermore, the thermal decomposition process of **3** has been intensively probed by the TG curve together with the variable-temperature PXRD patterns and variable-temperature IR spectra. This work shows that a great deal of rational structural design in the realm of organic–organic hybrid LSBs is possible. A further study will be carried out on utilizing other functionalized amino acid and multi-carboxylic ligands to sensitize the PL emission of Ln^{3+} cations and tune the magnetic interactions of Ln^{3+} cations, as well as exploiting the incorporation of TM cations to ulteriorly open up a new area in the heterometallic BT chemistry.

Acknowledgements

This work was supported by the Natural Science Foundation of China (21301049, U1304208, 21571048, 21671054), the Program for Science & Technology Innovation Talents in Universities of Henan Province (16HASTIT001), the Innovation Scientists and Technicians Troop Construction Projects of Henan Province, the Natural Science Foundation of Henan Province (142300410451), the Postdoctoral Foundation of Henan Province (20140025), the Foundation of State Key Laboratory of Structural Chemistry (20160016), the 2014 Special Foundation for Scientific Research Project of Henan University (XXJC20140001), the 2012 Young Backbone Teachers Foundation from Henan Province (2012GGJS-027) and the 2015, 2016 Students Innovative Pilot Plan of Henan University.

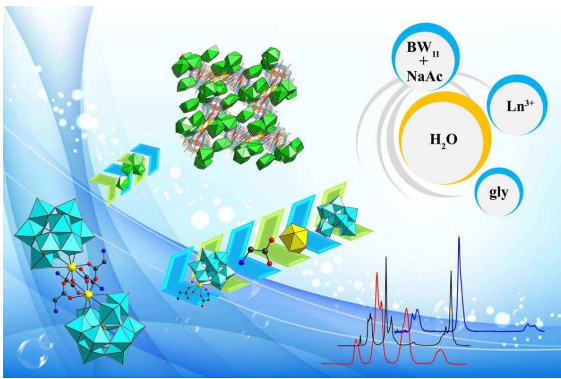
References

- ^aHenan Key Laboratory of Polyoxometalate Chemistry, Institute of Molecular and Crystal Engineering, College of Chemistry and Chemical Engineering, Henan University, Kaifeng, Henan 475004, P. R. China. Email: ljchen@henu.edu.cn, zhaojunwei@henu.edu.cn
- ^bState Key Laboratory of Structural Chemistry, Fujian Institute of Research on the Structure of Matter, Chinese Academy of Sciences, Fuzhou, Fujian 350002, P. R. China
- [†]Electronic Supplementary Information (ESI) available: IR spectra of **1–6** and $\text{K}_8[\alpha\text{-BW}_{11}\text{O}_{39}\text{H}]\cdot 13\text{H}_2\text{O}$, PXRD patterns of **1–6** and related structural figures; luminescence emission spectra and decay curves of **3–5** and $\text{K}_8[\alpha\text{-BW}_{11}\text{O}_{39}\text{H}]\cdot 13\text{H}_2\text{O}$; TG curves for **1–6**, and the variable temperature and PXRD spectra of **3**; BVS calculations of W, B and Ln atoms in **1–6**. For ESI and crystallographic data in CIF or other electronic format see DOI: 10.1039/b000000x/
- (a) I. V. Kozhevnikov, *Chem. Rev.*, 1998, **98**, 171; (b) A. Müller and F. Peters, *Chem. Rev.*, 1998, **98**, 239; (c) J. Zhou, J. W. Zhao, Q. Wei, J. Zhang and G. Y. Yang, *J. Am. Chem. Soc.*, 2014, **136**, 5065; (d) J. T. Rhule, C. L. Hill and D. A. Judd, *Chem. Rev.*, 1998, **98**, 327; (e) E. Coronado and C. J. Gómez-García, *Chem. Rev.*, 1998, **98**, 273; (f) S. G. Mitchell, C. Streb, H. N. Miras, T. Boyd, D. L. Long and L. Cronin, *Nat. Chem.*, 2010, **2**, 308; (g) Y. F. Wang and I. A. Weinstock, *Chem. Soc. Rev.*, 2012, **41**, 7479; (h) C. Fleming, D. L. Long, N. McMillan, J. Johnston, N. Bovet, V. Dhanak, N. Gadegaard, P. Kögerler, L. Cronin and M. Kadodwala, *Nat. Nanotechnol.*, 2008, **3**, 289.
- (a) V. E. Simmons and L. C. Baker, *W. Proc. VII I.C.C.C.*, Stockholm, 1962, 195; (b) L. C. W. Baker and V. E. Simmons, *Proc. IX I.C.C.C.*, St. Moritz, 1966, 421.
- G. A. Barbieri, *Atti. Accad. Nazi. Lincei*, 1914, **11**, 805.
- (a) R. D. Peacock and T. J. R. Weakley, *J. Chem. Soc. A*, 1971, 1836; (b) R. D. Peacock and T. J. R. Weakley, *J. Chem. Soc. A*, 1971, 1937.
- (a) K. Wassermann, M. H. Dickman and M. T. Pope, *Angew. Chem. Int. Ed. Engl.*, 1997, **36**, 1445; (b) F. Hussain, F. Conrad and G. R. Patzke, *Angew. Chem. Int. Ed.*, 2009, **48**, 9088; (c) W. M. Xuan, A. J. Surman, H. N. Miras, D. L. Long and L. Cronin, *J. Am. Chem. Soc.*, 2014, **136**, 14114; (d) J. Y. Niu, K. H. Wang, H. N. Chen, J. W. Zhao, P. T. Ma, J. P. Wang, M. X. Li, Y. Bai, and D. B. Dang, *Cryst. Growth Des.*, 2009, **9**, 4362; (e) M. K. Saini, R. Gupta, S. Parbhakar, A. K. Mishra, R. Mathurb and F. Hussain, *RSC Adv.*, 2014, **4**, 25357; (f) P. Mialane, A. Dolbecq, E. Rivière, J. Marrot and F. Sécheresse, *Eur. J. Inorg. Chem.*, 2004, **33**; (g) F. Hussain, A. Degonda, S. Sandriesser, T. Fox, S. S. Mal, U. Kortz and G. R. Patzke, *Inorg. Chim. Acta*, 2010, **363**, 4324; (h) U. Kortz, *J. Clust. Sci.*, 2003, **14**, 205; (i) M. Ibrahim, S. S. Mal, B. S. Bassil, A. Banerjee and U. Kortz, *Inorg. Chem.*, 2011, **50**, 956; (j) F. Hussain, R. W. Gable, M. Speldrich, P. Kögerler and C. Boskovic, *Chem. Commun.*, 2009, 328; (k) H. Y. An, Z. B. Han and T. Q. Xu, *Inorg. Chem.*, 2010, **49**, 11403; (l) C. Ritchie, E. G. Moore, M. Speldrich, P. Kögerler and C. Boskovic, *Angew. Chem. Int. Ed.*, 2010, **49**, 7702; (m) S. W. Zhang, Y. Wang, J. W. Zhao, P. T. Ma, J. P. Wang and J. Y. Niu, *Dalton Trans.*, 2012, **41**, 3764; (n) P. Mialane, A. Dolbecq, J. Marrot and F. Sécheresse, *Inorg. Chem. Commun.*, 2005, **8**, 740; (o) P. Mialane, A. Dolbecq and F. Sécheresse, *Chem. Commun.*, 2006, 3477; (p) F. Y. Li, W. H. Guo, L. Xu, L. F. Ma and Y. C. Wang, *Dalton Trans.*, 2012, **41**, 9220; (q) K. Wang, D. D. Zhang, J. C. Ma, P. T. Ma, J. Y. Niu and J. P. Wang, *CrystEngComm*, 2012, **14**, 3205; (r) Y. Wang, X. P. Sun, S. Z. Li, P. T. Ma, J. P. Wang and J. Y. Niu, *Dalton Trans.*, 2015, **44**, 733; (s) W. W. Ju, H. T. Zhang, X. Xu, Y. Zhang and Y. Xu, *Inorg. Chem.*, 2014, **53**, 3269; (t) N. Lotfian, M. Mirzaei, H. Eshtiagh-Hosseini, M. Löffler, M. Korabik and A. Salimi, *Eur. J. Inorg. Chem.*, 2014, 5908; (u) S. Z. Li, Y. Wang, P. T. Ma, J. P. Wang and J. Y. Niu, *CrystEngComm*, 2014, **16**, 10746; (v) Y. Wang, X. P. Sun, S. Z. Li, P. T. Ma, J. Y. Niu and J. P. Wang, *Cryst. Growth Des.*, 2015, **15**, 2057.
- (a) W. L. Chen, Y. G. Li, Y. H. Wang, E. B. Wang and Z. M. Su, *Dalton Trans.*, 2007, 4293; (b) X. J. Feng, H. Y. Han, Y. H. Wang, L. Li, Y. G. Li and E. B. Wang, *CrystEngComm*, 2013, **15**, 7267; (c) C. Ritchie and C. Boskovic, *Cryst. Growth Des.*, 2010, **10**, 488; (d) M. Vonci, F. A. Bagherjeri, P. D. Hall, R. W. Gable, A. Zavras, R. A. J. O'Hair, Y. P. Liu, J. Zhang, M. R. Field, M. B. Taylor, J. D. Plessis, G. Bryant, M. Riley, L. Sorace, P. A. Aparicio, X. López, J. M. Poblet, C. Ritchie and C. Boskovic, *Chem. Eur. J.*, 2014, **20**, 14102; (e) C. Ritchie, M. Speldrich, R. W. Gable, L. Sorace, P. Kögerler and C. Boskovic, *Inorg. Chem.*, 2011, **50**, 7004; (f) H. Naruke, J. Iijima and T. Sanji, *Inorg. Chem.*, 2011, **50**, 7535; (g) Y. J. Liu, H. L. Li, J. L. Zhang, J. W. Zhao and L. J. Chen, *Spectrochim. Acta Part A: Mol. Biomol. Spectr.*, 2015, **134**, 101.
- (a) F. L. Sousa, A. Ferreira, R. A. S. Ferreira, A. M. V. Cavaleiro, L. D. Carlos, H. I. S. Nogueira, J. Rocha and T. Trindade, *J. Nanosci. Nanotechnol.*, 2004, **4**, 214; (b) R. Ballardini, E. Chiorboli and V. Balzani, *Inorg. Chim. Acta*, 1984, **95**, 323; (c) N. Haraguchi, Y. Okaue, T. Isobe and Y. Matsuda, *Inorg. Chem.*, 1994, **33**, 1015; (d) H. Naruke and T. Yamase, *Bull. Chem. Soc. Jpn.*, 2000, **73**, 375; (e) F. L. Sousa, F. A. A. Paz, C. M. C. E. Granadeiro, A. M. V. Cavaleiro, J. Rocha, J. Klinowski and H. I. S. Nogueira, *Inorg. Chem. Commun.*, 2005, **8**, 924; (f) D. B. Dang, Y. Bai, C. He, J. Wang, C. Y. Duan and J. Y. Niu, *Inorg. Chem.*, 2010, **49**, 1280.
- (a) M. T. Pope, *Heteropoly and Isopoly Oxometalate*, Springer, Berlin, 1983, p. 79; (b) G. Hervé and A. C. R. Tézé, *Acad. Sci. Ser. C*, 1974, **278**, 1417.
- (a) A. Tézé, M. Michelon and G. Hervé, *Inorg. Chem.*, 1997, **36**, 505; (b) G. M. Maksimov, R. I. Maksimovskaya, G. S. Litvak and J. Russ, *Inorg. Chem.*, 2005, **50**, 1062; (c) N. Leclerc-Laronze, J. Marrot, G. Hervé, R. Thouvenot and E. Cadot, *Chem. Eur. J.*, 2007, **13**, 7234.
- F. A. Cotton and G. Wilkinson, *Advanced Inorganic Chemistry*, 4th ed., Wiley, New York, 1980, p. 296.
- (a) G. M. Sheldrick, *SHELXS 97, Program for Crystal Structure Solution*, University of Göttingen, Göttingen, Germany, 1997; (b) G.

- M. Sheldrick, *SHELXL 97, Program for Crystal Structure Refinement*, University of Göttingen, Germany, 1997.
- 12 J. W. Zhao, J. L. Zhang, Y. Z. Li, J. Cao and L. J. Chen, *Cryst. Growth Des.*, 2014, **14**, 1467.
- 13 (a) J. W. Zhao, J. Cao, Y. Z. Li, J. Zhang and L. J. Chen, *Cryst. Growth Des.*, 2014, **14**, 6217; (b) L. J. Chen, F. Zhang, X. Ma, J. Luo and J. W. Zhao, *Dalton Trans.*, 2015, **44**, 12598.
- 14 M. Sadakane, M. H. Dickman and M. T. Pope, *Angew. Chem. Int. Ed.*, 2000, **39**, 2914.
- 15 K. Suzuki, M. Sugawa, Y. Kikukawa, K. Kamata, K.; Yamaguchi and N. Mizuno, *Inorg. Chem.*, 2012, **51**, 6953.
- 16 S. Reinoso, P. Vitoria, L. S. Felices, L. Lezama and J. M. Gutierrez-Zorrilla, *Inorg. Chem.*, 2006, **45**, 108.
- 17 J. W. Zhao, H. L. Li, Y. Z. Li, C. Y. Li, Z. L. Wang and L. J. Chen, *Cryst. Growth Des.*, 2014, **14**, 5495.
- 18 (a) S. Reinoso, M. Giménez-Marqués, J. R. Galán-Mascarós, P. Vitoria and J. M. Gutiérrez-Zorrilla, *Angew. Chem. Int. Ed.*, 2010, **49**, 8384; (b) Z. M. Zhang, Y. G. Li, S. Yao and E. B. Wang, *Dalton Trans.*, 2011, **40**, 6475.
- 19 (a) J. Wang, J. W. Zhao, H. Y. Zhao, B. F. Yang, H. He and G. Y. Yang, *CrystEngComm*, 2014, **16**, 252; (b) S. Yao, Z. M. Zhang, Y. G. Li, Y. Lu, E. B. Wang and Z. M. Su, *Cryst. Growth Des.*, 2010, **10**, 135.
- 20 C. H. Li, K. L. Huang, Y. N. Chi, X. Liu, Z. G. Han, L. Shen and C. W. Hu, *Inorg. Chem.*, 2009, **48**, 2010.
- 21 (a) G. Blasse and B. C. Grabmaier, *Luminescent Materials*; Springer-Verlag: Berlin, 1994; (b) L. Armelao, S. Quici, F. Barigelletti, G. Accorsi, G. Bottaro, M. Cavazzini and E. Tondello, *Coord. Chem. Rev.*, 2010, **254**, 487; (c) M. D. Allendorf, C. A. Bauer, R. K. Bhakta and R. J. T. Houka, *Chem. Soc. Rev.*, 2009, **38**, 1330.
- 22 (a) Y. Q. Xiao, Y. J. Cui, Q. A. Zheng, S. C. Xiang, G. D. Qian and B. L. Chen, *Chem. Commun.*, 2010, **46**, 5503; (b) J. C. Boyer, M. P. Manseau, J. I. Murray and F. C. J. M. van Veggel, *Langmuir*, 2010, **26**, 1157; (c) E. Gaidamauskas, H. Parker, B. A. Kashemirov, A. A. Holder, K. Saejueng, C. E. McKenna and D. C. Crans, *J. Inorg. Biochem.*, 2009, **103**, 1652.
- 23 S. V. Eliseeva and J. C. G. Bunzli, *Chem. Soc. Rev.*, 2010, **39**, 189.
- 24 (a) M. Veith, C. Belot, V. Huch, H. L. Cui, L. Guyard, K. Michael and C. Wickleder, *Eur. J. Inorg. Chem.*, 2010, 879; (b) R. M. Abdelhameed, L. D. Carlos, A. M. S. Silva and J. Rocha, *Chem. Commun.*, 2013, **49**, 5019.
- 25 T. Fujii, K. Kodaira, O. Kawauchi, N. Tanaka, H. Yamashita and M. Anpo, *J. Phys. Chem. B*, 1997, **101**, 10631.
- 26 E. Cavalli, A. Belletti, R. Mahiou and P. Boutinaud, *J. Lumin.*, 2010, **130**, 733.
- 27 E. Álvarez, M. E. Zayas, J. Alvarado-Rivera, F. Félix-Domínguez, R. P. Duarte-Zamorano and U. Caldiño, *J. Lumin.*, 2014, **153**, 198.
- 28 (a) B. R. Judd, *Phys. Rev.*, 1962, **127**, 750; (b) G. S. J. Ofelt, *Chem. Phys.*, 1962, **37**, 511.
- 29 (a) A. F. Kirby and F. S. Richardson, *J. Phys. Chem.*, 1983, **87**, 2544; (b) J. W. Stouwdam and F. C. J. M. van Veggel, *Nano Lett.*, 2002, **2**, 733.
- 30 T. Zhang, C. Spitz, M. Antonietti and C. F. J. Faul, *Chem. Eur. J.*, 2005, **11**, 1001.
- 31 W. T. Xu, Y. F. Zhou, D. C. Huang, W. Xiong, M. Y. Su, K. Wang, S. Han and M. C. Hong, *Cryst. Growth Des.*, 2013, **13**, 5420.
- 32 S. J. Li, S. X. Liu, N. N. Ma, Y. Q. Qiu, J. Miao, C. C. Li, Q. Tang and L. Xu, *CrystEngComm*, 2012, **14**, 1397.
- 33 P. Mialane, L. Lissard, A. Mallard, J. Marrot, E. Antic-Fidancev, P. Aschehoug, D. Vivien and F. Sécheresse, *Inorg. Chem.*, 2003, **42**, 2102.
- 34 A. Beeby, I. M. Clarkson, R. S. Dickens, S. Faulkner, D. Parker, L. Royle, A. S. deSousa, J. A. G. Williams and M. Woods, *J. Chem. Soc. Perkin Trans.*, 1999, **2**, 493.
- 35 (a) B. D. Chandler, D. T. Cramb and G. K. H. Shimizu, *J. Am. Chem. Soc.*, 2006, **128**, 10403; (b) P. Mahata, K. V. Ramya and S. Natarajan, *Chem. Eur. J.*, 2008, **14**, 5839.
- 36 E. G. Moore, A. P. S. Samuel and K. N. Raymond, *Acc. Chem. Res.*, 2009, **42**, 542.
- 37 Y. Zhang, W. T. Gong, J. J. Yu, H. C. Pang, Q. Song and G. L. Ning, *RSC Adv.*, 2015, **5**, 62527.
- 38 M. L. Kahn, J. Sutter, S. Golhen, P. Guionneau, L. Ouahab, O. Kahn and D. Chasseau, *J. Am. Chem. Soc.*, 2000, **122**, 3413.
- 39 Y. Li, F. K. Zheng, X. Liu, W. Q. Zou, G. C. Guo, C. Z. Lu and J. S. Huang, *Inorg. Chem.*, 2006, **45**, 6308.
- 40 C. Benelli and D. Gatteschi, *Chem. Rev.*, 2002, **102**, 2369.
- 41 B. Liu, B.-L. Li, Y.-Z. Li, Y. Chen, S.-S. Bao and L.-M. Zheng, *Inorg. Chem.*, 2007, **46**, 8524.
- 42 Z. H. Zhang, T. Okamura, Y. Hasegawa, H. Kawaguchi, L. Y. Kong, W. Y. Sun and N. Ueyama, *Inorg. Chem.*, 2005, **44**, 6219.
- 43 C. J. Milios, P. A. Wood, S. Parsons, D. Foguer-Albiol, C. Lampropoulos, G. Christou, S. P. Perlepes and E. K. Brechin, *Inorg. Chim. Acta*, 2007, **360**, 3932.
- 44 (a) F. Ferraro and R. Arratia-Pérez, *Polyhedron*, 2011, **30**, 860; (b) V. N. Nikiforov, Y. A. Koksharov, A. V. Gribanov, M. Baran and V. Y. J. Irkhin, *Magn. Mater.*, 2015, **383**, 215.
- 45 K. Y. Cui, F. Y. Li, L. Xu, B. B. Xu, N. Jiang, Y. C. Wang and J. P. Zhang, *Dalton Trans.*, 2012, **41**, 4871.
- 46 T. Arumuganathan and S. K. Das, *Inorg. Chem.*, 2009, **48**, 496.
- 47 F. He, M. L. Tong, X. L. Yu and X. M. Chen, *Inorg. Chem.*, 2005, **44**, 559.

First quadruple-glycine bridging mono-lanthanide-substituted borotungstate hybrids

Jiancai Liu, Jing Yu, Qing Han, Yue Wen, Lijuan Chen,* and Junwei Zhao*



A class of novel organic–inorganic hybrid quadruple-glycine lanthanide-substituted Keggin-type borotungstates have been synthesized and characterized.